

The Impact of Magnons, Defects, and Rapid Energy Migration on the Optical Properties of the 2D Magnet CrPS₄

Jacob T. Baillie,¹ Eden Tzanetopoulos,¹ Rachel T. Smith,¹
Remi Beaulac,² and Daniel R. Gamelin^{1,*}

¹*Department of Chemistry, University of Washington, Seattle, WA 98195*

²*Department of Chemistry, Swarthmore College, Swarthmore, PA 19081*

*Contact author: gamelin@uw.edu

Abstract. Strong coupling between optical and magnetic excitations could enable contactless, spatially resolved, or ultrafast interrogation and control of magnetism two-dimensional (2D) materials and devices. The layered 2D A-type antiferromagnet CrPS₄ stands out among van der Waals (vdW) magnets for its rich optical fine structure, but its spectroscopy is not yet understood and has so far been interpreted without consideration of magnetic exchange. Here, we show that this fine structure comes primarily from exchange-mediated coupling between on-site optical "spin-flip" transitions of Cr³⁺ and low-energy spin transitions involving the surrounding lattice. Well-resolved magnon sidebands to optical ⁴A₂ ↔ ²E transitions are observed in photoluminescence (PL) and PL excitation spectra, as well as a pronounced PL sideband due to short-range exchange splitting. Energy migration is probed using Yb³⁺ dopants as traps, revealing sub-picosecond inter-site excitation hopping. Formation of dispersive Frenkel excitons of coupled on-site *d-d* transitions due to inter-site exchange is discussed. In addition to impacting how optical fine structure is interpreted in this and potentially other vdW magnets, these findings may have ramifications for future applications of layered 2D magnets by revealing new opportunities to drive mode-specific spin-wave excitations using light.

I. Introduction

The emergence of two-dimensional (2D) van der Waals (vdW) magnets has stimulated advances in the fundamental physics of strongly correlated systems as well as the development of nascent nanoscale spintronic technologies.^{1, 2} Magnetic vdW materials have proven to be effective platforms for exploring purely magnetic phenomena, including layer-dependent magnetism,^{3, 4} the generation or transport of spin waves,⁵⁻⁹ and spin-dependent tunneling.¹⁰⁻¹² Intrinsic coupling between optical and magnetic properties in such materials has further introduced avenues for contactless, spatially resolved, or ultrafast interrogation of magnetism^{3, 13-20} and, in some cases,

optical control of spin orientation.²¹⁻²³ In three-dimensional magnetic materials, such coupling has already been used for spin-photon transduction in optical isolators, magnetic sensors, and memory devices.²⁴⁻²⁶ 2D magnets can offer analogous functionality with thicknesses down to atomic length scales in a form that is readily interfaced with incommensurate materials through hetero-stacking. In some 2D magnets, such as the workhorse CrX_3 ($X = \text{Cl, Br, I}$) compounds, optical transitions are broadened by strong electron-phonon coupling, obscuring the interplay between the optical and magnetic properties. In other materials, such as CrPS_4 and CrSBr , narrow optical transitions are observed with complex fine structure that is not fully understood. A deeper fundamental understanding of the optical properties and electronic structures of such materials will enable their full potential to be tapped for future applications.

Here, we present a detailed description of the optical properties of the A-type layered antiferromagnet, CrPS_4 . CrPS_4 is an emerging 2D material whose unique magnetic and optical properties have only recently begun to be understood and exploited.²⁷⁻³⁶ Figure 1a depicts the stacked lattice structure of CrPS_4 and the structure of one individual layer. The individual layer is highly anisotropic, with linear chains of edge-sharing Cr^{3+} octahedra running along the crystallographic b axis. Parallel chains are separated by the S–P–S linkages of bridging $[\text{PS}_4]^{3-}$ moieties. Magnetic susceptibility^{31, 32} and neutron diffraction³⁰ experiments on bulk CrPS_4 have established A-type antiferromagnetic (A-AFM) ordering below a Néel temperature (T_N) of ~ 36 K, in which each monolayer orders ferromagnetically (FM) with all Cr^{3+} moments oriented nearly perpendicular to the 2D plane, and these monolayers stack with opposite spin orientations to form the extended A-AFM lattice. Its structural anisotropy lends CrPS_4 a quasi-one-dimensional (1D) electronic structure that is manifested in disproportionately strong b -axis magnetic exchange coupling,³⁰ anisotropic magnon^{8, 9} and charge³⁷ transport, and primarily b -polarized absorption,^{33, 38} reflectance,²⁸ and PL²⁹ spectra. Interplay between the magnetic and optical properties of CrPS_4 has been found in magneto-PL experiments^{29, 36} and sensitivity of the PL intensity to temperature near T_N .^{29, 34}

Despite these promising results, the optical properties and electronic structure of CrPS_4 remain poorly defined, particularly pertaining to the luminescent excited state. Several^{28, 29, 34-36, 39-44} publications have interpreted the absorption, PL, reflectance, and photoconductivity spectra in terms of localized ligand-field electronic transitions from individual Cr^{3+} ions (illustrated in Figure 1b). The low-temperature PL of CrPS_4 occurs at $\sim 10970 \text{ cm}^{-1}$ (1.36 eV) and has been assigned to

${}^2E \rightarrow {}^4A_2$ ligand-field emission,^{34, 35} but the decay time of this PL is reportedly < 1 ns,³⁵ whereas 2E emission typically decays on micro- to millisecond timescales due to the transition's spin-forbiddenness. A pronounced vibronic progression in the PL spectrum has been described,^{29, 34-36} and additional unusual fine structure has been attributed^{29, 34, 43} to a Fano-type resonant coupling of the ${}^2E \rightarrow {}^4A_2$ transition with a separate atom-like oscillator, proposed to be excess atomic phosphorous within the lattice. Critically, the impact of magnetic exchange on the CrPS₄ PL spectrum has not been addressed. Additionally, to date, no absorption or PLE spectra have been reported for the ${}^4A_2 \rightarrow {}^2E$ energy region that could test current interpretations.

In this study, we analyze the PL spectra of CrPS₄, complemented by absorption, high-resolution PLE, PL quantum yield, and time-resolved PL data, and we present a revised interpretation of the fine structure of these spectra by explicitly accounting for magnetic exchange. We identify the electronic origins of the ${}^4A_2 \leftrightarrow {}^2E$ transition in PL and PLE measurements at $E({}^2E) \approx 11069$ cm⁻¹ (1.372 eV) based on mirrored fine structure. From PL quantum-yield measurements, we are able to attribute the unusually fast 2E decay to rapid nonradiative trapping, and using time-resolved PL, we identify emission from a native "defect" Cr³⁺ site with a microsecond lifetime. Using Yb³⁺ dopants as "designer" defects for capturing excitation energy from CrPS₄, time-resolved and variable-temperature PL measurements allow the conclusion of sub-picosecond site-to-site energy-hopping times, indicating that this excited state is a weakly dispersive Frenkel exciton. We identify several resolved magnon sidebands in the PL and PLE fine structure at low temperature, showing that exciton-magnon coupling is an important source of ${}^2E \rightarrow {}^4A_2$ PL intensity. Finally, we observe an additional relatively intense PL feature that is redshifted from the first ${}^2E \rightarrow {}^4A_2$ electronic origin and that can be assigned to a spin-conserving pure-electronic transition terminating at an excited spin level of the exchange-split ground state. This transition serves as the origin of the most prominent phonon replicas in the PL spectra of CrPS₄. This work helps to establish CrPS₄ as a model system for the fundamental understanding of spin effects in the optical spectra of magnetic van der Waals compounds. Furthermore, the identification of well-resolved magnetic sidebands in CrPS₄ absorption and PL spectra reveals new opportunities to explore and harness coupling between optical excitations and spin waves in layered magnetic materials.

II. Results and Analysis

General Characterization. CrPS₄ crystals were grown *via* chemical vapor transport. X-ray

diffraction (XRD) and Raman spectroscopy data collected on single-crystal flakes align well with reference data (Figure S1). In the XRD pattern, the (00 l) peaks are relatively more intense than in the reference pattern, reflecting orientation of the flake with its c -axis normal to the substrate. Field-cooled (FC) and zero-field-cooled (ZFC) magnetic susceptibility (χ) measurements (Figure S2) confirm the A-type antiferromagnetism (A-AFM) reported previously.³¹ Further details are provided in the Methods section and as Supplementary Materials.

Spectroscopic Overview. Figure 1c shows unpolarized room-temperature and 18 K absorption spectra collected through a thin (52 ± 7 μm) CrPS₄ single crystal, with light propagating along the crystallographic c axis. Molar extinction coefficients (ϵ) were determined using the Beer-Lambert law based on the flake thickness, the Cr³⁺ density in the lattice, and the measured optical density (Figure S3). The broad absorption band at 14000 cm^{-1} (1.736 eV, at 18 K) is assigned to the spin-allowed $^4\text{A}_2 \rightarrow ^4\text{T}_2$ ligand-field transition of the pseudo-octahedral Cr³⁺. The peak extinction coefficient of this band is 16 ± 2 $\text{M}^{-1}\text{cm}^{-1}$, which is reasonable for octahedral Cr³⁺.⁴⁵ A similar extinction coefficient was measured for an ensemble of CrPS₄ microcrystals prepared by sonication (Figure S3). This band narrows when the crystal is cooled to 18 K, attributed to the loss of vibronic hot bands. The absorption maximum shifts to higher energy at lower T , consistent with the known Cr–S bond-length contraction in CrPS₄.^{30, 46} A series of more intense bands is observed at higher energies in the sonicated CrPS₄ microcrystals (Figure S3), with strong absorption beginning above ~ 18000 cm^{-1} . The first peak maximum in this region occurs at ~ 19500 cm^{-1} (2.418 eV) and is assigned to a ligand-to-metal charge-transfer (LMCT) transition.³⁹

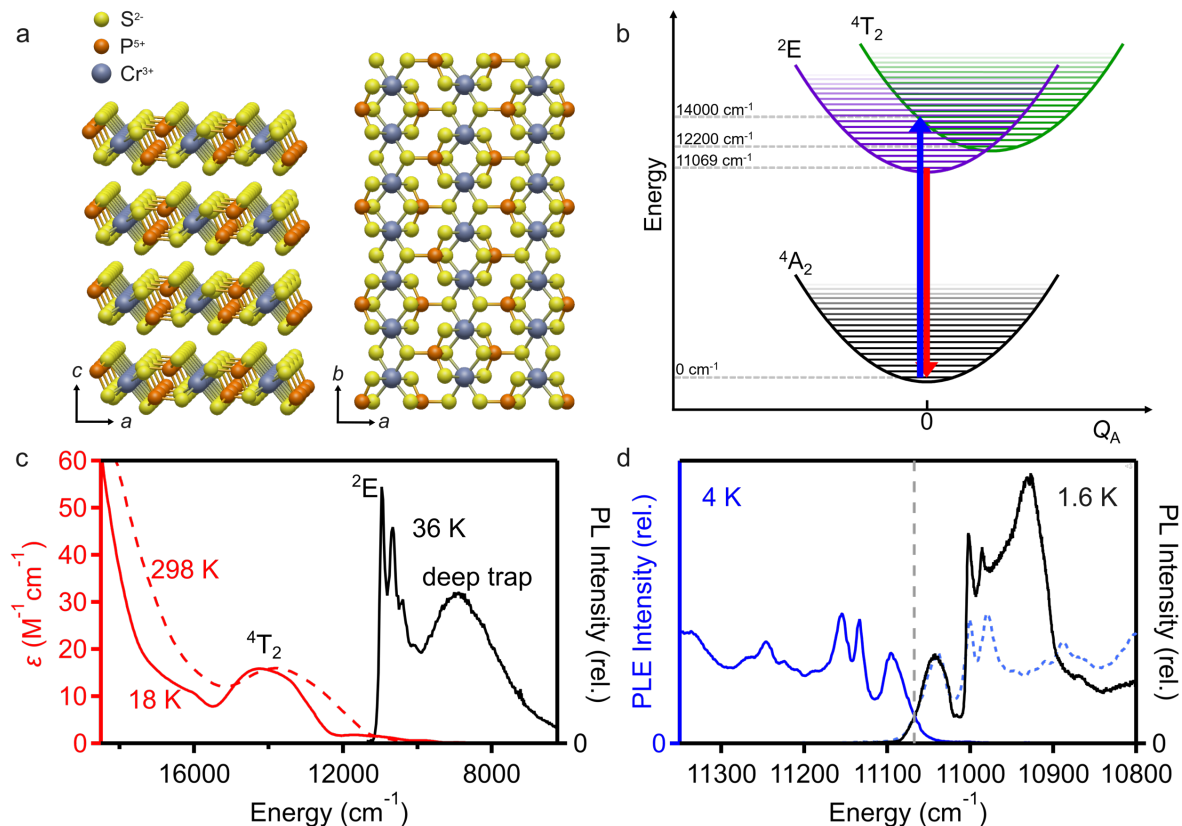


Figure 1. (a) Images of the structure of CrPS₄ based on the data in ref 46. (b) Configurational coordinate diagram (along the totally symmetric nuclear coordinate) representing the localized *d-d* transitions of an octahedral *d³* Cr³⁺ ion in CrPS₄ at 4 K. The blue arrow represents one of the vibronic transitions of the 4A₂ → 4T₂ absorption and the red arrow represents the electronic origin of the 2E → 4A₂ luminescence. (c) Absorption spectra of a 52 ± 7 μm thick CrPS₄ single crystal (~70k layers, Figure S3) at 298 K (dashed red) and 18 K (solid red), collected using unpolarized light propagating along the crystallographic *c* axis. 36 K PL spectrum of a CrPS₄ single crystal (black) collected using pulsed 21277 cm⁻¹ photoexcitation (470 nm, unpolarized, 2.5 MHz, 3 ns pulse duration, 6.3 nJ pulse energy). A 1 nm (~10 cm⁻¹) spectral bandwidth was used for detection. Extinction coefficients represent the average in-plane values and are estimated to be accurate to within ±14%. (d) 1.6 K PL spectrum of a CrPS₄ single crystal (black) and 4 K PLE spectrum of a 0.2% Yb³⁺:CrPS₄ single crystal (blue). The PL spectrum was collected using continuous-wave (CW) 15803 cm⁻¹ photoexcitation (633 nm, unpolarized, 5 mW/cm²). A 0.05 nm (~0.5 cm⁻¹) spectral bandwidth was used for detection. The PLE spectrum was collected by photoexciting with a tunable, CW Ti:sapphire laser (unpolarized, 5–50 mW/cm², 0.1 nm linewidth) while monitoring PL at 9302 cm⁻¹ (spectral bandwidth = ±22 cm⁻¹, see Figure S9). For reference, the PLE spectrum is also shown flipped (dotted light blue) across the dashed gray line at 11069 cm⁻¹.

Figure 1c also shows the 36 K PL spectrum of a CrPS₄ single crystal. A series of evenly spaced peaks is observed near 10500 cm⁻¹ that has been attributed to vibronic coupling in the localized 2E excited state.^{29, 34–36} The broad feature near 9000 cm⁻¹ has been assigned to deep-trap PL.^{23, 35} The

2E PL intensity is nearly linearly dependent on excitation power ($I \propto P^{1.08}$, Figure S4), whereas this deep-trap PL shows $I \propto P^{0.76}$ (Figure S4), indicating saturation. The relatively low excitation power densities used in this work ($< 2 \text{ W/cm}^2$) compared with the previous report of this feature ($\sim 3 \text{ kW/cm}^2$)³⁵ may explain why this deep-trap PL appears relatively more intense here. Overall, the 36 K PL spectrum is consistent with literature reports. The results and analysis presented below focus on understanding the CrPS₄ PL and absorption (or PLE) spectra in the region of the first electronic excitations.

Low-Temperature Absorption (or PLE) and PL. Figure 1d shows the PL spectrum of a CrPS₄ single crystal measured at 1.6 K together with a 4 K laser PLE spectrum, expanded around the highest-energy 2E PL peak of Figure 1c. The PL spectrum shows extensive fine structure, as discussed previously,^{29, 34, 36, 43, 44} with its first three peak maxima at 11042, 11002, and 10986 cm^{-1} . This fine structure shows negligible dependence on excitation position within the crystal (Figure S5), excitation energy (Figures S6 and S7), or excitation power (Figure S6), and it shows very little flake-to-flake variability (Figure S8). The CrPS₄ PLE spectrum was collected at 4 K using a 0.2% Yb³⁺-doped CrPS₄ (Yb³⁺:CrPS₄) single crystal (see Figure S9 for PL). Although there is no significant difference in CrPS₄ PLE fine structure near the PL origin between Yb³⁺:CrPS₄ and CrPS₄ samples (Figure S10), Yb³⁺ doping provides much greater PL quantum yields²³ and consequently greater signal-to-noise in the PLE measurements. This PLE spectrum mostly resembles the PL spectrum mirrored across a midpoint energy of 11069 cm^{-1} (1.372 eV, dashed gray line in Figure 1d), with its first three peak maxima at 11096, 11134, and 11155 cm^{-1} . These data indicate that the fine structure in both excitation and emission is built upon a common pure-electronic origin at ca. 11069 cm^{-1} . Absorption at this energy is very weak, with $\epsilon < \sim 0.5 \text{ M}^{-1}\text{cm}^{-1}$ (Figure S11). This small extinction coefficient is characteristic of spin-forbidden ligand-field transitions of Cr³⁺ and supports the assignment of this absorption and PL to the $^4A_2 \leftrightarrow ^2E$ electronic transition of Cr³⁺. The more intense, broader absorption band centered at 14000 cm^{-1} (Figure 1c) is assigned as the first spin-allowed ligand-field transition, $^4A_2 \rightarrow ^4T_2$, broadened slightly by the presence of two Cr³⁺ lattice sites and the fact that each has low symmetry. This band is also observed in extended PLE spectra (see Supplementary Materials, Figures S10 and S11). Relevant energies are included in Figure 1b.

The observation of 2E absorption before the onset of 4T_2 absorption demonstrates that Cr³⁺ in CrPS₄ resides in a strong ligand-field environment at 4 K. From ligand-field theory for octahedral

Cr^{3+} , $E(^4\text{T}_2) = 10Dq$, such that $Dq = 1400 \text{ cm}^{-1}$ in CrPS_4 . Diagonalization of the 4×4 matrix of ^2E energies gives as the lowest root $E(^2\text{E})/B \approx 3.05 C/B + 7.09 - 1.80 B/Dq$,^{47, 48} where B and C are the Racah parameters describing electron-electron repulsion. No other ligand-field excited states could be identified below the charge-transfer onset, so B and C cannot both be determined experimentally. Using the experimental energy $E(^2\text{E}) = 11069 \text{ cm}^{-1}$ and a typical ratio of $C/B = 4.5$ for Cr^{3+} compounds yields $B = 551 \text{ cm}^{-1}$ and hence $Dq/B \sim 2.54$. This value is greater than previously estimated ($Dq/B \sim 2.08$),³⁴ and it demonstrates that Cr^{3+} is further from the excited-state spin-crossover point at 4 K than previously thought. Perhaps more importantly, the large reduction of B from its free-ion value ($B_0 = 933 \text{ cm}^{-1}$)⁴⁹ has not yet been commented upon. This reduction results from Cr^{3+} $3d$ covalency, which diminishes electron-electron repulsion through the nephelauxetic effect.^{45, 50} Large ranges in the value of C/B for Cr^{3+} ions have been quoted in recent literature,⁵¹ and consequently the usual nephelauxetic parameter $\beta = B/B_0$ appears poorly correlated with $E(^2\text{E})$ in many Cr^{3+} compounds.⁵² To minimize uncertainty from assumption of a specific C/B ratio, we may instead express the reduction of electron-electron repulsion in terms of the "new" nephelauxetic parameter, β_1 , described in ref 52 and defined in eq 1a (using free-ion $B_0 = 933 \text{ cm}^{-1}$ and $C_0 = 3732 \text{ cm}^{-1}$ from ref 49).

$$\beta_1 = \sqrt{\left(\frac{B}{B_0}\right)^2 + \left(\frac{C}{C_0}\right)^2} \quad (1a)$$

To normalize relative to the free ion, we redefine this parameter as in eq 1b. Note that if $C/B = C_0/B_0$ then $\kappa = \beta$.

$$\kappa = \frac{1}{\sqrt{2}} \sqrt{\left(\frac{B}{B_0}\right)^2 + \left(\frac{C}{C_0}\right)^2} \quad (1b)$$

For CrPS_4 at 4 K, $\kappa = 0.62$, which is essentially independent of the assumed C/B ratio. This value of κ is low even for sulfide-coordinated Cr^{3+} . For example, $\kappa = 0.67$ for Cr^{3+} doped into the thiospinel, ZnAl_2S_4 .⁵³ Consequently, the ^2E energy is lower in CrPS_4 than in Cr^{3+} -doped ZnAl_2S_4 (11069 vs 12970 cm^{-1}). We attribute the high Cr^{3+} d -orbital covalency in CrPS_4 to the high polarizability of the $[\text{PS}_4]^{3-}$ anion and the low coordination number of the sulfides that occupy the

out-of-plane Cr^{3+} coordination sites; each sulfide in ZnAl_2S_4 is 4-coordinate, whereas in CrPS_4 the four bridging sulfides are 3-coordinate and the two out-of-plane sulfides are only 2-coordinate. With the above ligand-field parameters ($Dq = 1400 \text{ cm}^{-1}$, $B = 551 \text{ cm}^{-1}$, $C/B = 4.5$), the $^4\text{A}_2 \rightarrow ^4\text{T}_1(\text{F})$ transition in CrPS_4 is expected to occur at $\sim 19500 \text{ cm}^{-1}$, where it would be obscured by charge-transfer absorption (Figure 1c).

Variable-Temperature ^2E Absorption (PLE) and PL. Figure 2 replots the low-temperature PL spectrum of Figure 1d together with additional PL and PLE data collected at various temperatures up to 105 K. In the low-temperature PL spectra, evenly spaced PL and PLE peaks are indicated with gray or light blue lines. The $\sim 300 \text{ cm}^{-1}$ spacing between these replicas can be attributed to the A_6 phonon mode (Figure S1b), whose Raman scattering is polarized in the ab plane.^{54, 55} This mode is expected^{56, 57} to be centered around Cr^{3+} rather than P and may thus couple more strongly than others to the $^4\text{A}_2 \leftrightarrow ^2\text{E}$ transition. The coupling is not strong, with the Huang-Rhys parameter estimated to be $S \sim 0.5$, depending on the choice of baseline. As the temperature increases, the PL and PLE peaks broaden and the relative peak intensities change dramatically. In the 4 K and 16 K PL spectra, three prominent peaks are observed near 10750 cm^{-1} , well below the PL origin at 11069 cm^{-1} . Upon close inspection, these peaks are also weakly evident in the 1.6 K PL spectrum. These three peaks show the same splitting and intensity pattern as the highest-energy peaks centered around 10960 cm^{-1} . In fact, each of these peaks occurs exactly $208 \pm 1 \text{ cm}^{-1}$ below the corresponding member of the first set (Figure S12). Moreover, 300 cm^{-1} replicas associated with these new peaks are also identifiable (blue lines in Figure 2). Due to this nearly identical fine structure, we interpret this 10750 cm^{-1} PL as ^2E emission from a "defect" Cr^{3+} site, an interpretation borne out by time-resolved PL measurements discussed below. The similar fine structure is expected because the $^2\text{E} \rightarrow ^4\text{A}_2$ emission of such defect Cr^{3+} sites can couple similarly to phonons and magnons (see below), as observed in, *e.g.*, YCrO_3 .⁵⁸ By 36 K, the PL and PLE fine structure is no longer resolved; only the 300 cm^{-1} progression is observed, and these features continue broadening with increasing temperature. Given the very strong temperature dependence of this PL spectrum at low temperatures, the many inconsistencies among previously reported^{23, 29, 34-36, 43, 44} low-temperature CrPS_4 PL spectra are likely primarily attributable to variations in laboratory sample temperature.

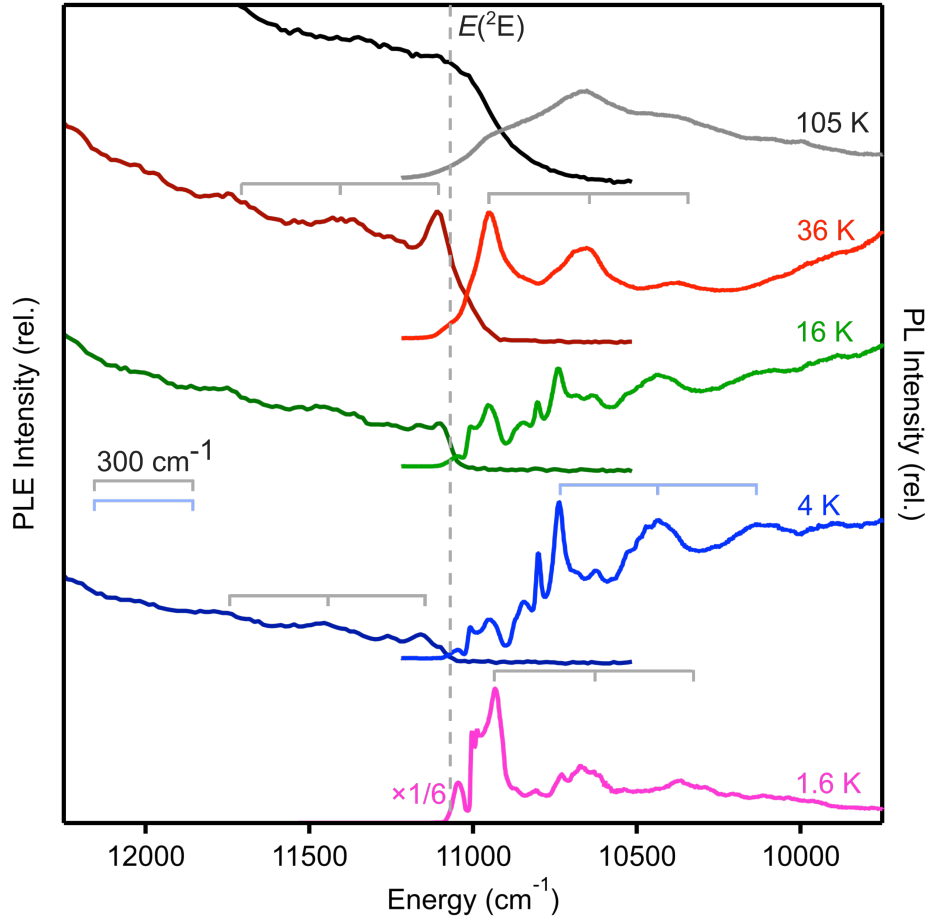


Figure 2. Variable-temperature PL spectra of CrPS₄ single crystals (lighter colors) and PLE spectra of a 0.2% Yb³⁺:CrPS₄ single crystal (darker colors). PL and PLE spectra for $T = 4, 16, 36, 105$ K are from the same single crystal measured in a closed-cycle cryostat. A different crystal was used for the $T = 1.6$ K measurements in a helium immersion cryostat. Spectra were collected using CW 15803 cm⁻¹ photoexcitation (633 nm, unpolarized, 5 mW/cm²). A 0.05 nm (~ 0.5 cm⁻¹) spectral bandwidth was used for detection. The dashed gray line indicates $E(^2E) = 11069$ cm⁻¹ in the low-temperature limit. Bars are drawn for the first two replicas of each component at select temperatures as a guide to the eye. The spacing is 300 cm⁻¹. PLE spectra were collected by photoexciting with a CW halogen lamp (10-50 μ W/cm², 1 nm linewidth) while monitoring PL at 9302 (spectral bandwidth ± 22 cm⁻¹, see Figure S9).

An important consideration when assessing variable-temperature PL data is the PLQY (Φ), which quantifies the competition between radiative and nonradiative relaxation processes. The total PLQY was measured for several CrPS₄ flakes at room temperature using an integrating sphere, yielding an average value of $\Phi_{\text{tot}} = \sim 0.14\%$. From this value and full spectral measurements performed between room temperature and 4 K (Figures S13-S16), we can determine that $\Phi_{\text{tot}} = \sim 0.5\%$ below 60 K. Thus, the PLQY of CrPS₄ is very low at all temperatures.

Furthermore, by analysis of the spectral data to omit the deep-trap and defect Cr^{3+} (near 10750 cm^{-1} , *vide infra*) PL intensities, the PLQY for just the intrinsic ${}^2\text{E} \rightarrow {}^4\text{A}_2$ component of the PL spectrum can also be determined, giving $\Phi_{{}^2\text{E}} < 0.1\%$ at all temperatures. These results indicate that CrPS_4 photoexcitation is overwhelmingly followed by nonradiative deactivation, rather than by PL. Changes in absolute PL intensities with parameters such as temperature therefore most likely reflect changes in the dynamics of nonradiative processes and require cautious interpretation.

Time-Resolved PL. More can be learned from studying the PL spectrum in the time domain. Figure 3 shows time-resolved PL data measured in the ${}^2\text{E} \rightarrow {}^4\text{A}_2$ region at different temperatures. At 4 K, two PL components are identified that have very different decay times. The short-time data are dominated by a "Fast" component with $\tau_{\text{fast}} \sim 2\text{ ns}$ and with intensity originating at $\sim 10960\text{ cm}^{-1}$. At longer times, a much slower component is observed, originating at $\sim 10750\text{ cm}^{-1}$. Separate measurements with a slower excitation repetition rate show that this "Slow" PL has a decay time of $\tau_{\text{slow}} \sim 7\text{ }\mu\text{s}$ at 4 K. The 2.5 nm ($\sim 25\text{ cm}^{-1}$) spectral bandwidth used for detection in this experiment causes instrument-limited linewidths, but the features are easily correlated with those in the CW spectra measured at higher resolution (Figures 1 and 2). Based on its relationship to the PLE onset (Figure 2), the "Fast" PL corresponds to the majority species in CrPS_4 , such that we can associate it with the ${}^2\text{E}$ luminescence from the lattice Cr^{3+} ions ($\tau_{\text{fast}} \equiv \tau_{{}^2\text{E}}$). The absence of PLE intensity near the onset of the "Slow" PL (Figures 1d, 2) allows assignment of this "Slow" PL to a rarer "defect" Cr^{3+} ($\tau_{\text{slow}} \equiv \tau_{\text{defectCr}}$). Defect PL in fully concentrated Cr^{3+} lattices commonly stems from the occurrence of native defects that perturb the energies of proximal lattice Cr^{3+} ions. Microcrystalline CrPS_4 powder prepared by sonication shows the same defect Cr^{3+} PL (Figure S17), suggesting that it is associated with native bulk defects rather than surface or edge defects.

The bottom panels of Figure 3 show time-gated PL spectra extracted by integrating the time-resolved data over the first 5 ns (0–5 ns, lattice ${}^2\text{E}$) and over a later 5 ns window (145–150 ns, defect Cr^{3+}). As noted above, the defect Cr^{3+} spectrum is very similar to the lattice ${}^2\text{E}$ spectrum, just shifted to lower energy by 208 cm^{-1} and having distinct temperature and time dependencies. Overall, these results demonstrate that the CrPS_4 PL spectrum derives some of its complexity from the presence of ${}^2\text{E}$ emission from two Cr^{3+} species: regular lattice sites and defect sites.

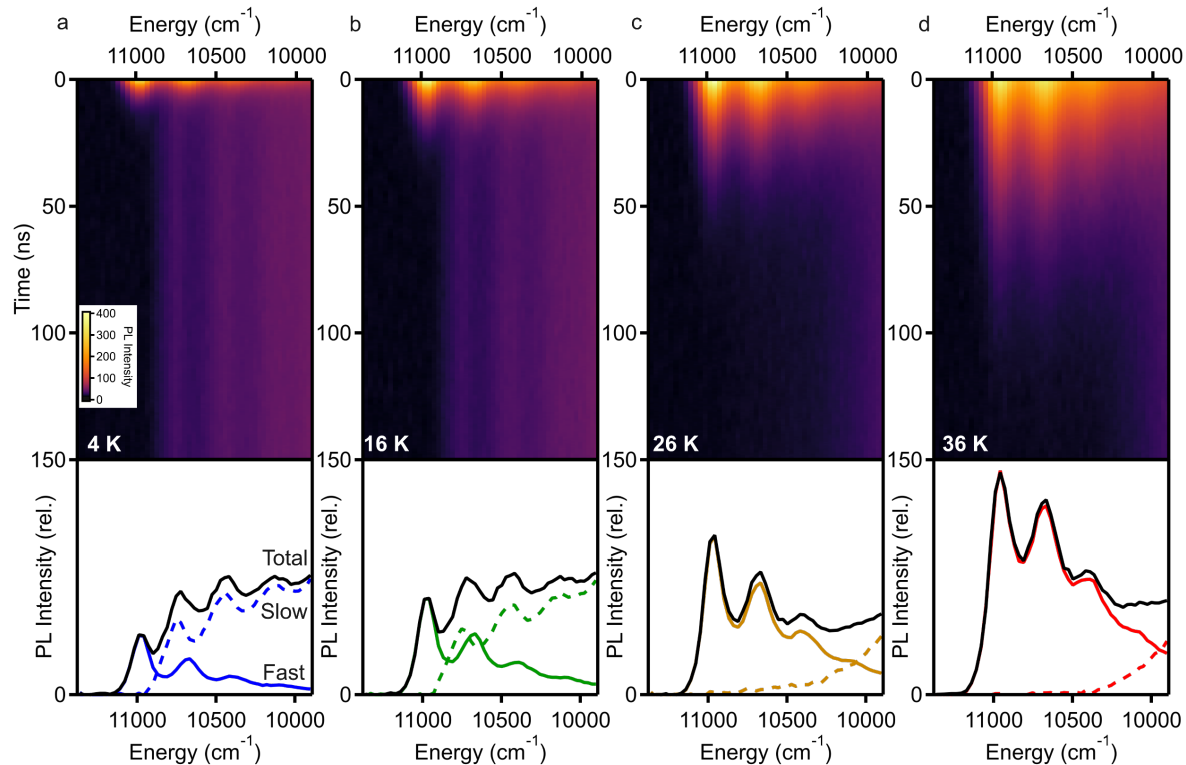


Figure 3. (a) Top: 4 K false-color plot of the PL decay vs energy measured across the region of the ${}^2E \rightarrow {}^4A_2$ transition with a 2.5 nm ($\sim 25 \text{ cm}^{-1}$) spectral bandwidth. Bottom: PL spectra obtained by integrating across all time (I_{total} , “Total”, black), over the first 5 ns ($I_{0-5 \text{ ns}} - I_{145-150 \text{ ns}}$, intrinsic lattice 2E , solid), and over a later 5 ns window ($I_{145-150 \text{ ns}}$, defect Cr^{3+} , dashed). The lattice 2E and defect Cr^{3+} spectra are scaled so their sum equals I_{total} . (b-d) Same as panel (a) but measured at 16, 26, and 36 K, respectively. All data are for a CrPS_4 single crystal and collected using pulsed 21277 cm^{-1} photoexcitation (470 nm, 2.5 MHz, 3 ns pulse duration, 6.3 nJ pulse energy).

Figure 4 summarizes the decay dynamics of the intrinsic lattice 2E and defect Cr^{3+} PL components. The lattice 2E PL decays monoexponentially with $\tau_{{}^2E} = 1.7 \text{ ns}$ at 4 K, slowing to $\tau_{{}^2E} = 6.0 \text{ ns}$ at 24 K (Figure 4a). The full temperature dependence of $\tau_{{}^2E}$ up to 60 K (Figure 4b) shows a gradual increase with increasing temperature over this range. The opposite temperature dependence is observed in Figure 4c for the slow defect Cr^{3+} PL, whose decay accelerates from $\tau_{\text{defectCr}} \sim 7 \text{ } \mu\text{s}$ at 4 K to $0.7 \text{ } \mu\text{s}$ at 24 K. Figure 4d shows that τ_{defectCr} changes little at low temperatures up to $\sim 16 \text{ K}$, at which point it drops rapidly with increasing temperature. Additional data detailing the distinct temperature dependencies of these two PL signals are provided in the Supplementary Materials (Figures S18-S20).

Using the PL quantum yields described above (Figure S16), it is possible to analyze these decay

dynamics to estimate the radiative and nonradiative rate constants (k_r and k_{nr} , respectively) for decay of the lattice 2E population at each temperature using eqs 2 and 3 (see Figure S21).

$$k_r = \Phi_{^2E} \cdot k_{^2E} = \tau_r^{-1} \quad (2)$$

$$k_{nr} = k_{^2E} - k_r \quad (3)$$

This analysis suggests a radiative lifetime of $\tau_r = 7 \mu s$ at 4 K for the lattice 2E PL, which coincidentally is similar to the experimental value of $\tau_{\text{defectCr}} = 7 \mu s$ at 4 K. Although the very low PLQY may cause uncertainty in the precise radiative lifetime deduced here, slow radiative decay is already anticipated from the small extinction coefficients of the corresponding absorption transitions (*e.g.*, $\varepsilon < \sim 0.5 \text{ M}^{-1}\text{cm}^{-1}$ at 11069 cm^{-1}). Note that the low-temperature radiative decay is accelerated by spin effects that have no counterpart in the low-temperature absorption (see below), allowing faster radiative decay than anticipated from the absorption spectrum alone. Overall, this analysis shows that the short PL decay times widely observed near the absorption edge of CrPS₄ are primarily due to *nonradiative* processes, and the radiative lifetimes of these transitions are instead on the order of microseconds.

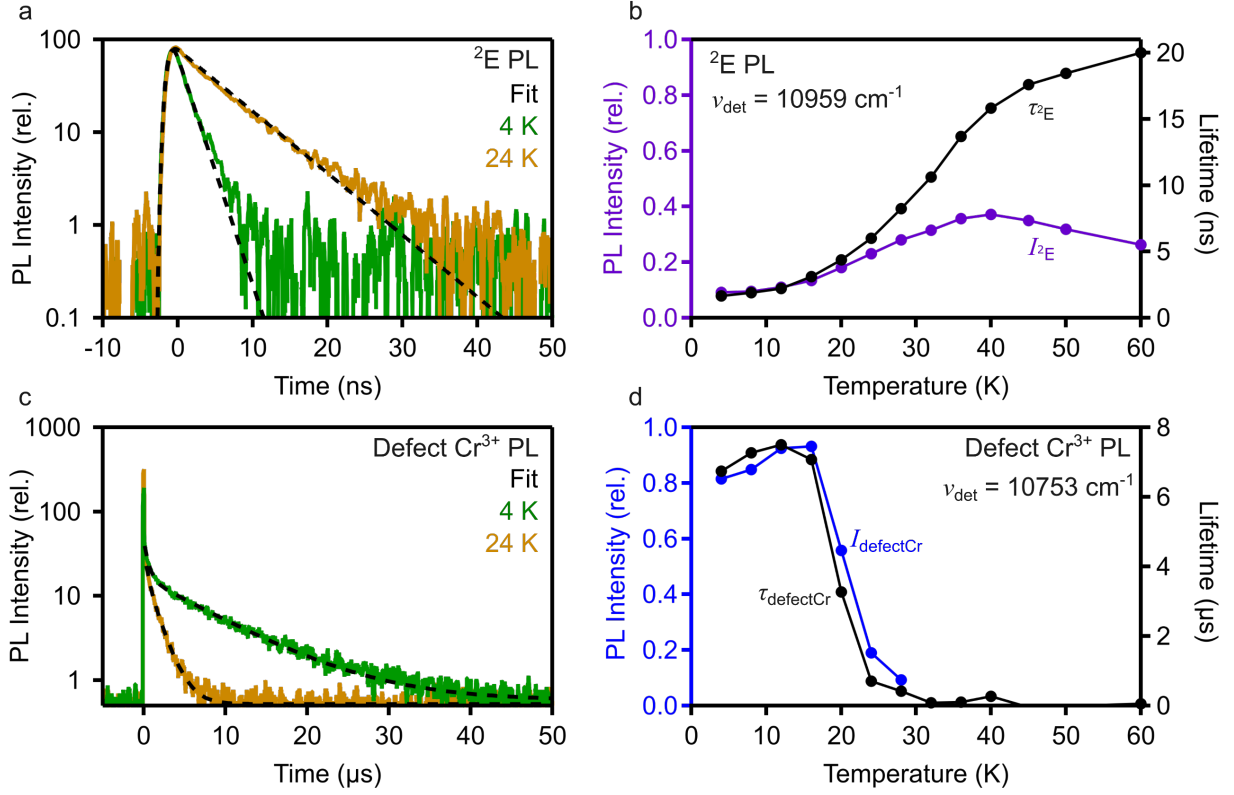


Figure 4. (a) 4 K (green) and 24 K (orange) PL decay curves of the intrinsic lattice 2E PL at a detection energy (ν_{det}) of 10959 (spectral bandwidth $\pm 15 \text{ cm}^{-1}$) collected using pulsed 21277 cm^{-1} photoexcitation (470 nm, unpolarized, 2.5 MHz, 3 ns pulse duration, 6.3 nJ pulse energy). $\tau_{^2E}$ is determined by fitting to the convolution of the modeled monoexponential and the instrument response function (IRF) using nonlinear least-squares regression (dashed black, see Figure S18 for fitting details). (b) Temperature dependence of $I_{^2E}$ from panel (a) (purple) and the corresponding PL decay time (black). (c) 4 K (green) and 24 K (orange) PL decay curves of the slow defect Cr^{3+} PL at 10753 (spectral bandwidth $\pm 14 \text{ cm}^{-1}$) collected by photoexciting with the pulsed 18797 cm^{-1} (532 nm) output of a frequency-doubled Nd:YAG laser (unpolarized, 50 Hz, 30 ps pulse duration, 4 μJ pulse energy). The illustrated fits (dashed black) are biexponential decays starting from $t = 50 \text{ ns}$ to avoid temporal overlap with the fast lattice 2E PL. τ_{defectCr} is determined using eq S1. (d) Temperature dependence of I_{defectCr} from panel (a) (blue, integrated over 0.05–75 μs) and the corresponding defect Cr^{3+} PL decay time (black).

With this consideration in mind, Figure 4d plots the temperature dependence of the defect Cr^{3+} PL intensities (I_{defectCr} , obtained by integrating decay data) together with the temperature dependence of the defect Cr^{3+} PL decay times, for comparison with Figure 4b. Similar trends for $I_{^2E}$ and I_{defectCr} are obtained from variable-temperature CW PL spectra (Figure S22). The data in Figure 4b show that $\tau_{^2E}$ tracks $I_{^2E}$ at low temperature, diverging somewhat above 28 K. Similarly, τ_{defectCr} tracks I_{defectCr} closely, both dropping to nearly zero above 16 K. Notably, the 2E and defect

Cr^{3+} data do *not* track one another, with $\tau_{^2E}$ and $I_{^2E}$ changing more gradually over a broader temperature range than τ_{defectCr} and I_{defectCr} , indicating that these processes are not correlated in any straightforward way. These results confirm that this temperature dependence is dominated by changes in nonradiative processes.

We note that the same two PL signals and their different dependence on temperature were previously identified in CW PL measurements and assigned to the two low-symmetry-split spin-orbit components of the same 2E state of the majority lattice Cr^{3+} species.³⁴ Two observations argue against this interpretation: (i) the PLE data in Figure 2 show massively different excitation rates for the two emissive levels, with the lower-energy level not even detectable, whereas the two 2E spinors of Cr^{3+} should have similar absorption cross sections, and (ii) the time-resolved PL data in Figure 3 demonstrate that these two emissive states are not in thermal equilibrium with one another under any of our measurement conditions, as they should be for two 2E sublevels of the same Cr^{3+} ion. These considerations support assignment of the PL originating at $\sim 10750 \text{ cm}^{-1}$ to a separate minority "defect" Cr^{3+} site.

Energy Migration and Exciton Dispersion. Recently, we reported that doping CrPS_4 with Yb^{3+} leads to efficient sensitization of Yb^{3+} luminescence even at low Yb^{3+} concentrations.²³ We now capitalize on this property by using Yb^{3+} dopants to assess the dynamics of energy migration within the lattice. To illustrate, Figure 5a shows 36 K PL spectra of CrPS_4 crystals grown with and without Yb^{3+} ($\text{Yb}_x\text{Cr}_{1-x}\text{PS}_4$). With only $x = 0.002$, the CrPS_4 PL described above is almost completely replaced by narrow-line Yb^{3+} f - f emission centered at $\sim 9600 \text{ cm}^{-1}$, and the total PLQY (Φ'_{tot}) increases $\sim 50\times$, now exceeding 25% above $\sim 30 \text{ K}$ (Figures S23 and S24). This large increase in PLQY with doping reinforces the conclusion drawn above that the lattice Cr^{3+} PL in CrPS_4 is strongly suppressed by nonradiative processes. The Yb^{3+} PL accounts for $\sim 97.6\%$ of all emission from this sample at 4 K, rising to $>98.1\%$ at 30 K and above. The shape of the lattice 2E PL remains very similar to that of undoped CrPS_4 (Figure S22) regardless of x . These observations indicate rapid energy migration among lattice sites, analysis of which can provide information about the intrinsic luminescent excited state(s) of CrPS_4 , which to date has been described as a localized 2E state of a single Cr^{3+} ion.

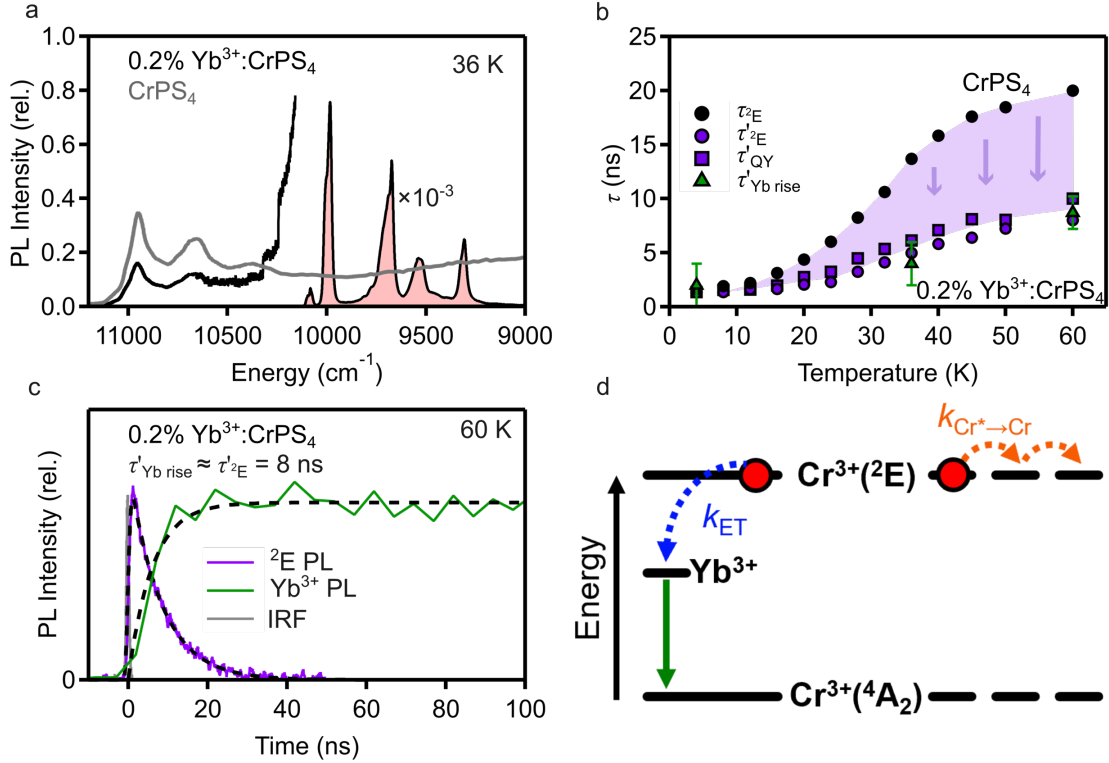


Figure 5. (a) 36 K PL spectrum of a single crystal of 0.2% Yb³⁺:CrPS₄ (black, redrawn from Figure 2) relative to the PL intensities at 298 K (Figure S13). (b) Temperature dependence of τ_{2E} (black circles, undoped, replotted from Figure 4b), τ'_{2E} (purple circles, doped), τ'_{QY} (purple squares, doped) *cf.* eq 4, and $\tau'_{Yb\ rise}$ (green triangles with error bars). (c) 60 K time-resolved Yb³⁺ PL curve of 0.2% Yb³⁺:CrPS₄ measured at 10959 (spectral bandwidth (sbw) ± 15 cm⁻¹) by omitting the deep-trap PL (green) collected by photoexciting with the pulsed 18797 cm⁻¹ (532 nm) output of a frequency-doubled Nd:YAG laser (unpolarized, 50 Hz, 30 ps pulse duration, 4 μ J pulse energy). The data are fitted (dashed black) to a monoexponential rise ($\tau'_{Yb\ rise} = 8.7$ ns) and monoexponential decay ($\tau'_{Yb\ decay} = 83$ μ s). 60 K intrinsic lattice 2E PL decay curve of 0.2% Yb³⁺:CrPS₄ measured at 9302 (sbw ± 11 cm⁻¹, purple) collected and fitted (dashed black, $\tau'_{2E} = 8.0$ ns) as described in Figure 4a. (d) Illustration of the kinetic parameters discussed in the main text: k_{ET} denotes the phenomenological CrPS₄ \rightarrow Yb³⁺ energy-transfer rate constant, and $k_{Cr^* \rightarrow Cr}$ denotes the microscopic $Cr^{3+*} \rightarrow Cr^{3+}$ excitation hopping rate constant.

Time-domain PL measurements were used to learn more about energy migration in CrPS₄. Figure 5b compares Cr^{3+} PL decay times (τ'_{2E}) measured for 0.2% Yb³⁺:CrPS₄ with those for the same lattice 2E emission of undoped CrPS₄ (τ_{2E} from Figure 4b). Both decay times increase with increasing temperature in a similar way, but PL decay is $\sim 2\times$ faster in the doped sample, indicating that energy transfer from CrPS₄ to Yb³⁺ (k_{ET}) occurs on the same timescale as the PL decay (~ 2 ns at 4 K). Figure 5c plots time-resolved Yb³⁺ PL measured at 60 K after pulsed excitation of the CrPS₄ lattice and omitting the trap PL (see Figures S26 and S27). The PL does not decay

immediately but instead shows a distinct rise at short times. The fitted rise time of $\tau'_{\text{Yb rise}} = 8.7$ ns agrees well with the lattice ^2E PL decay time measured under the same conditions ($\tau'_{^2\text{E}} = 8.0$ ns). $\tau'_{\text{Yb rise}}$ values measured in this way at 4, 36, and 60 K are plotted in Figure 5b and track the Cr^{3+} ^2E decay data precisely. Very similar results are also obtained from analysis of the change in lattice Cr^{3+} ^2E PLQY upon Yb^{3+} doping, as described by eq 4 and plotted as τ'_{QY} in Figure 5b. From these data, we can directly attribute the decrease of the lattice ^2E PL decay time and quantum yield upon Yb^{3+} doping to capture of excitation energy by Yb^{3+} .

$$\tau'_{\text{QY}} = \tau_{^2\text{E}} \cdot \frac{\Phi'_{^2\text{E}}}{\Phi_{^2\text{E}}} \quad (4)$$

At such low Yb^{3+} doping levels, the CrPS_4 excitation typically occurs some distance from any Yb^{3+} , and energy migration within the lattice is required before capture by Yb^{3+} . To analyze the microscopic Cr^{3+} – Cr^{3+} hopping rate constant ($k_{\text{Cr}^* \rightarrow \text{Cr}}$), we first determine the phenomenological $\text{CrPS}_4 \rightarrow \text{Yb}^{3+}$ energy-transfer rate constant (k_{ET}) based on the Inokuti–Hirayama treatment of donor decay modified by energy transfer (eq 5).^{59, 60}

$$k_{\text{ET}} = \frac{1}{\tau'_{^2\text{E}}} - \frac{1}{\tau_{^2\text{E}}} \quad (5)$$

k_{ET} decreases with increasing temperature from 0.15 ns^{-1} at 4 K to 0.07 ns^{-1} at 60 K (Figure S25a). Similar results are obtained when using PL quantum yields to calculate k_{ET} (eq 6, see Figure S25a).

$$k_{\text{ET}} = \frac{1}{\tau_{^2\text{E}}} \cdot \left(\frac{\Phi_{^2\text{E}}}{\Phi'_{^2\text{E}}} - 1 \right) \quad (6)$$

For energy migration dominated by the strong intra-chain coupling between Cr^{3+} ions at the smallest Cr^{3+} – Cr^{3+} distances (relative to inter-chain or inter-layer coupling over larger distances), a microscopic rate constant for diffusive 1-D hopping ($k_{\text{Cr}^* \rightarrow \text{Cr}}$) can be estimated from the Yb^{3+} concentration dependence of k_{ET} as described by eq 7.^{61, 62}

$$k_{\text{ET}} = k_{\text{Cr}^* \rightarrow \text{Cr}} [4x]^2 \quad (7)$$

From eq 7 and the 4 K value of $k_{ET} = 0.15 \text{ ns}^{-1}$ for 0.2% $\text{Yb}^{3+}:\text{CrPS}_4$, we obtain $k_{\text{Cr}^* \rightarrow \text{Cr}} = 2.4 \text{ ps}^{-1}$. Similar values are obtained for all Yb^{3+} concentrations examined here (Figure S25). We note that because $k_{\text{Cr}^* \rightarrow \text{Cr}}$ is determined from energy capture at low Yb^{3+} doping concentrations, where energy-migration lengths are large, it represents an effective value despite the presence of two crystallographic Cr^{3+} sites. Figure 5d illustrates $k_{\text{Cr}^* \rightarrow \text{Cr}}$ and k_{ET} , summarizing the exciton dynamics analyzed here. Overall, these data indicate sub-picosecond Cr^{3+} – Cr^{3+} hopping times.

This inter-site hopping in CrPS_4 is extremely fast compared with that determined for CrI_3 ($k_{\text{Cr}^* \rightarrow \text{Cr}} \sim 10 \text{ } \mu\text{s}^{-1}$),⁶³ where hopping is slowed by strong electron-nuclear coupling in the emissive $^4\text{T}_2$ excited state. This hopping is too fast to be mediated by multipolar coupling,^{64, 65} and instead, it is attributed to inter-site exchange (Dexter-type energy transfer). Substantial Cr^{3+} – Cr^{3+} exchange coupling is evident from the magnetic ordering of CrPS_4 . Importantly, with this coupling, excited states consisting of just one Cr^{3+} ion in its ^2E excited state are no longer eigenstates of the periodic lattice, and instead the eigenstates are Frenkel excitons comprising symmetrized linear combinations of single-ion ^2E excited states. This coupling gives rise to exciton dispersion and, in materials hosting translationally inequivalent neighboring ions, Davydov-type resonant energy splittings at the Brillouin-zone center ($\mathbf{k} = 0$).⁶⁶⁻⁶⁸ The inequivalent neighboring Cr^{3+} ions in CrPS_4 show much stronger coupling than the equivalent next-nearest-neighbors, and ^2E energies are ligand-field independent, so the Davydov splittings (ΔE_{Dav}) should provide a good measure of the total exciton dispersion energy (ΔE_{band}).⁶⁸

Experimentally, Davydov splittings are not resolved in either our PL or laser PLE measurements, but their magnitude can be estimated from consideration of the experimental energy migration rates measured above. In a symmetrical Cr^{3+} Frenkel dimer, ΔE_{Dav} is related to the coherent inter-site energy-transfer rate constant k_{transfer} as described by eq 8,^{47, 69}

$$\Delta E_{\text{Dav}} = \left(\frac{h}{2}\right) k_{\text{transfer}} \quad (8)$$

where h is Planck's constant. Extension to an infinite linear chain is described by eq 9.⁷⁰

$$\Delta E_{\text{Dav}} = \left(\frac{h}{4}\right) k_{\text{transfer}} \quad (9)$$

From eq 9 and assuming $k_{\text{transfer}} = k_{\text{Cr}^* \rightarrow \text{Cr}} = 2.4 \text{ ps}^{-1}$ at 4 K, a value of $\Delta E_{\text{Dav}} \sim 20 \text{ cm}^{-1}$ would be estimated for the ^2E exciton of CrPS_4 at this temperature. ΔE_{Dav} is thus small, and even this value is likely an overestimation. A more precise estimate of ΔE_{Dav} would require accounting for the presence of two lattice sites, vibronic coupling, and any common structural disorder in the lattice. These factors all favor excitation localization and loss of coherence, opposing the dispersive electron-exchange interactions. Additionally, the roles of inter-chain or inter-layer hopping may be underestimated by assuming a linear-chain model.

Exciton-Magnon Coupling and Other Spin Effects. Mirrored fine structure between absorption and PL spectra of transition-metal ions is commonly observed due to electron-nuclear coupling, where vibronic transitions appear as sidebands to pure electronic transitions. Such a picture is described well by ligand-field theory and has already been discussed for CrPS_4 ,^{28, 29, 34-36, 39-44} but this picture is only adequate for isolated transition-metal ions. For CrPS_4 , the optical spectra are also expected to show concrete manifestations of inter-ion magnetic exchange coupling. In particular, coupling of $^4\text{A}_2 \leftrightarrow ^2\text{E}$ spin-flip transitions with dispersive magnons introduces a new mechanism for conserving spin angular momentum, and therefore generating electric-dipole allowedness in the optical transitions.^{68, 71-75} Tanabe and coworkers^{76, 77} have detailed an exchange mechanism by which spin-forbidden $d-d$ transitions of exchange-coupled ions can gain electric-dipole allowedness. The dominant terms contributing to electric-dipole intensity in this mechanism involve the same inter-ion one-electron transfer processes as in the ground-state magnetic-exchange coupling. This "Tanabe mechanism" is responsible for intensification of $^4\text{A}_2 \leftrightarrow ^2\text{E}$ transitions in the optical spectra of exchange-coupled Cr^{3+} pairs in doped crystals and molecules, following the pair spin selection rules $\Delta S = 0$ and $\Delta M_S = 0$, where S is the total pair spin (S_{pair}), and it also accounts well for the properties of ions in fully concentrated magnetic crystals.⁷⁶⁻⁸⁰ When exciton dispersion is small, as found here, the magnetically activated sidebands should closely resemble the magnon density of states (DOS), with intensities weighted by the momentum-resolved coupling strength.

To investigate whether any of the fine structure in the PL or PLE spectra of CrPS_4 derives from magnetic exchange, the magnon DOS was calculated (see Methods). The magnetic Hamiltonian used here is given by eq 9,

$$\mathcal{H} = -2J_1 \sum_{i,j} \mathbf{S}_i \cdot \mathbf{S}_j - 2J_2 \sum_{i,k} \mathbf{S}_i \cdot \mathbf{S}_k - 2J_3 \sum_{i,l} \mathbf{S}_i \cdot \mathbf{S}_l - 2J_c \sum_{i,m} \mathbf{S}_i \cdot \mathbf{S}_m - \sum_{i,z} D_z (S_i^z)^2 \quad (9)$$

where J_n are the magnetic exchange coupling parameters and D_z is the effective Cr^{3+} single-ion anisotropy. The relevant J_n values were obtained from experimental inelastic neutron scattering data³⁰ (accounting for the use of a $+J$ Hamiltonian in the source publication). Figure 6a replots the low-temperature PL and PLE spectra from Figure 1d with the magnon DOS superimposed in both absorption and emission directions, taking the dashed vertical line as the common pure-electronic origin. The magnon DOS maxima, calculated with no adjustable parameters, align remarkably well with the low-energy fine-structure peaks observed in both PL and PLE. This comparison provides strong evidence that the *majority* of this fine structure indeed comes from exciton-magnon coupling. We note that some of this fine structure in the PL spectrum was previously interpreted in terms of a Fano-type resonance involving coupling of single-ion ^2E PL to an atom-like defect transition,^{29, 34, 43} but the mirroring of this structure in the PLE spectrum indicates otherwise, and prediction of this structure from the magnon DOS calculation provides a more compelling interpretation. Importantly, all of the magnon DOS maxima in Figure 6a stem from dispersion primarily along the crystallographic b direction. For example, the pair of peaks $\sim 80 \text{ cm}^{-1}$ from the origin is a signature of the magnon DOS gap that is formed by having two alternating J values along the b -oriented 1D chains (J_1 and J_2). Because the primary source of electric-dipole intensity in this transition involves magnetic exchange, the magnetic anisotropy of CrPS_4 is ultimately responsible for the optical polarization along b .

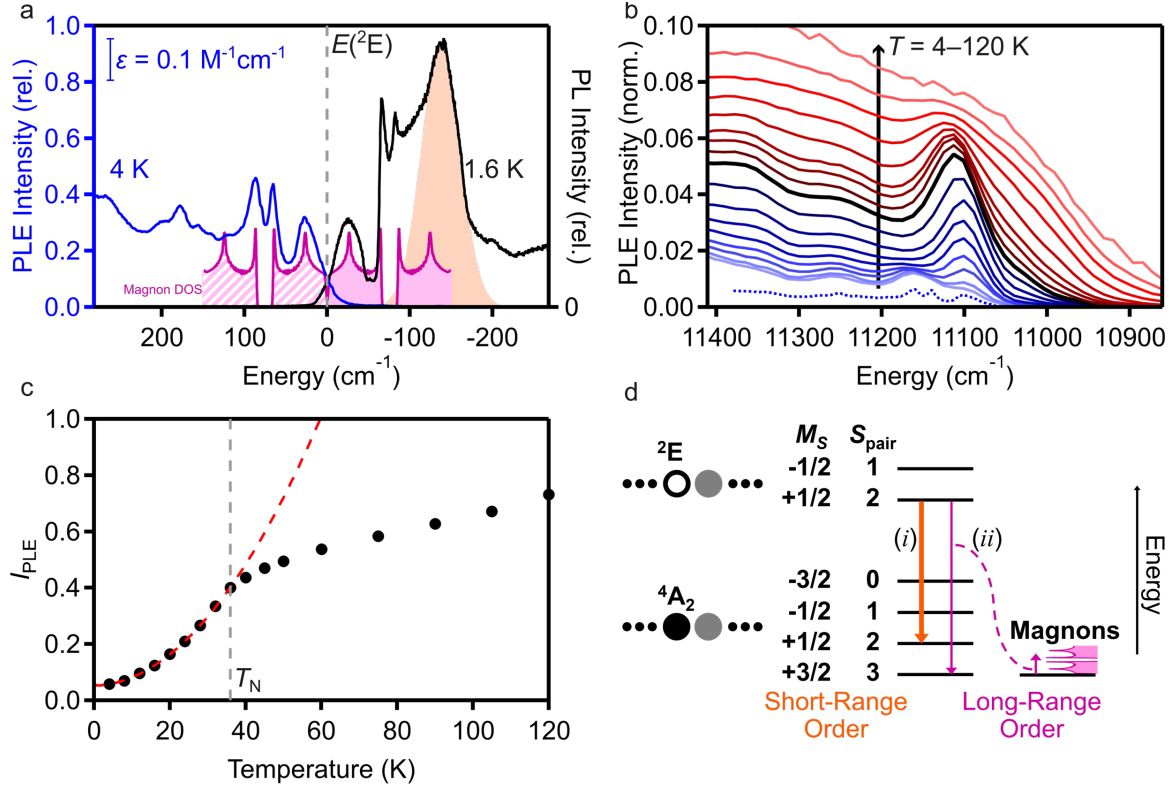


Figure 6. (a) 1.6 K PL (black) and 4 K PLE (blue) spectra redrawn from Figure 1c and offset to center $E(^2E)$ at zero (gray dashed line). The magnon DOS (magenta, arb. scaling) is plotted to positive (partial fill) and negative (solid fill) energies. The spin-preserving $^2E(+1/2, 2) \rightarrow ^4A_2(+1/2, 2)$ transition is shaded orange. The scale bar indicates the molar extinction coefficient (ϵ), determined from absorption spectroscopy (see Figures 1c and S11). (b) Variable-temperature PLE spectra of exfoliated 0.2% $\text{Yb}^{3+}:\text{CrPS}_4$ crystals on clear adhesive tape (see Methods) in the region of the $^4A_2 \rightarrow ^2E$ transition. Spectra are collected using a CW halogen lamp for photoexcitation ($10\text{--}50 \mu\text{W}/\text{cm}^2$, 1 nm linewidth) with Yb^{3+} PL detection at $9302 \text{ (sbw } \pm 22 \text{ cm}^{-1})$ and normalized to the maximum PLE intensity of the $^4A_2 \rightarrow ^4T_2$ transition (Figure S28). The 36 K spectrum is emphasized (thick black). The high-resolution PLE spectrum from panel (a) is redrawn for comparison (dashed blue). (c) Integrated PLE intensity of the $^4A_2 \rightarrow ^2E$ transition vs temperature from the data in panel (b). Data were integrated from $11000\text{--}11200 \text{ cm}^{-1}$. The dashed curve describes T^2 temperature dependence described by eq 10. (d) Schematic depiction of an exchange-coupled Cr^{3+} pair within an extended CrPS_4 linear chain. Electronic excitation localized around one ion of the pair is depicted. Energy diagram describing the two exchange-mediated spin-conserving PL mechanisms identified in the $\text{Cr}^{3+} ^2E \rightarrow ^4A_2$ fine structure of CrPS_4 : (i) a $^2E(+1/2, 2) \rightarrow ^4A_2(+1/2, 2)$ transition that preserves the total spin and spin projection *via* short-range magnetic order within pairs, and (ii) magnon-assisted transitions that couple the spin-forbidden $^2E(+1/2, 2) \rightarrow ^4A_2(+3/2, 3)$ transition to compensating spin-wave excitations (long-range order). Energies not to scale.

An interesting aspect of these data is that magnon sidebands are observed at energies of both $E(^2E) + E(\text{magnon})$ (in PLE) and $E(^2E) - E(\text{magnon})$ (in PL) at the lowest measurement

temperature. The observation by PLE of such magnon sidebands would be unexpected for monolayer CrPS₄, because long-range ferromagnetic spin correlation at the lowest temperature precludes magnon creation that *increases* spin angular momentum to offset the loss of spin angular momentum in the $^4A_2 \rightarrow ^2E$ optical excitation. Such processes do become possible in layered CrPS₄, however, due to the antiferromagnetic *inter*-layer coupling. In contrast, the magnon sidebands in the low-temperature PL spectrum can be assigned to *intra*-layer magnon creation with optical excitation.

Additional evidence of exciton-magnon coupling is observed in variable-temperature PLE measurements. Figure 6b plots PLE spectra collected while monitoring the Yb³⁺ *f-f* PL of a 0.2% Yb³⁺:CrPS₄ flake. To eliminate any internal temperature dependence of the Yb³⁺ PL, these PLE intensities are plotted relative to the 4T_2 peak maximum of each PLE spectrum (Figure S28), based on the observation in Figure 1c (and Figure S29) that 4T_2 absorption changes little over this temperature range (as expected for a spin-allowed transition in low symmetry). The narrowest linewidths in these spectra are instrument-limited (see Figure 6a), but the trends are nonetheless apparent: as the temperature increases from 4 K, the 2E PLE intensity increases dramatically and its structure broadens. Figure 6c plots the temperature dependence of this PLE intensity integrated from 11000–11200 cm⁻¹, showing that it increases rapidly above 4 K. This strong temperature dependence continues until $T_N \sim 36$ K and then abruptly changes to a weaker temperature dependence, demonstrating that it is linked to magnetic order. Indeed, this temperature dependence is very similar to that observed in the magnetic exchange splittings of Yb³⁺ dopant PL lines in CrPS₄ (Figure S28d).²³

Microscopically, this PLE temperature dependence from 4 K – T_N reflects the introduction of new spin-conserving transitions that couple Cr³⁺ $^4A_2 \rightarrow ^2E$ excitation with hot-magnon deexcitation. The data are described well in terms of the loss of long-range spin correlation in CrPS₄ *via* thermal magnon excitation, following the expected T^2 dependence described by eq 10.⁸¹

$$I(T) = I_0 + AT^2 \exp\left(\frac{-\Delta_0}{k_B T}\right) \quad (10)$$

Here, I_0 is the intensity at 0 K, A is a scalar, Δ_0 is the spin-wave gap (1.05 cm⁻¹ (0.13 meV) measured in ref 30), and k_B is the Boltzmann constant. Because $\Delta_0 \ll k_B T$ in all measurements,

this temperature dependence essentially follows T^2 . This process is thus similar to the hot magnon sidebands of optical spin-flip transitions in easy-plane A_2CrCl_4 layered ferromagnets.^{82, 83} Magnons coupled to $^4A_2 \rightarrow ^2E$ excitations must all *increase* the lattice spin projection, and in the low-temperature limit of $CrPS_4$ this can only be achieved by exciting magnons across the van der Waals gap. Raising the temperature introduces the possibility of coupling with primarily *intra*-layer hot magnons, and the large PLE intensity increase in Figure 6b,c indicates that this is a more effective intensity-gaining mechanism than inter-layer magnon coupling, consistent with the dependence of electric-dipole intensity on exchange-coupling strength outlined in the Tanabe mechanism.

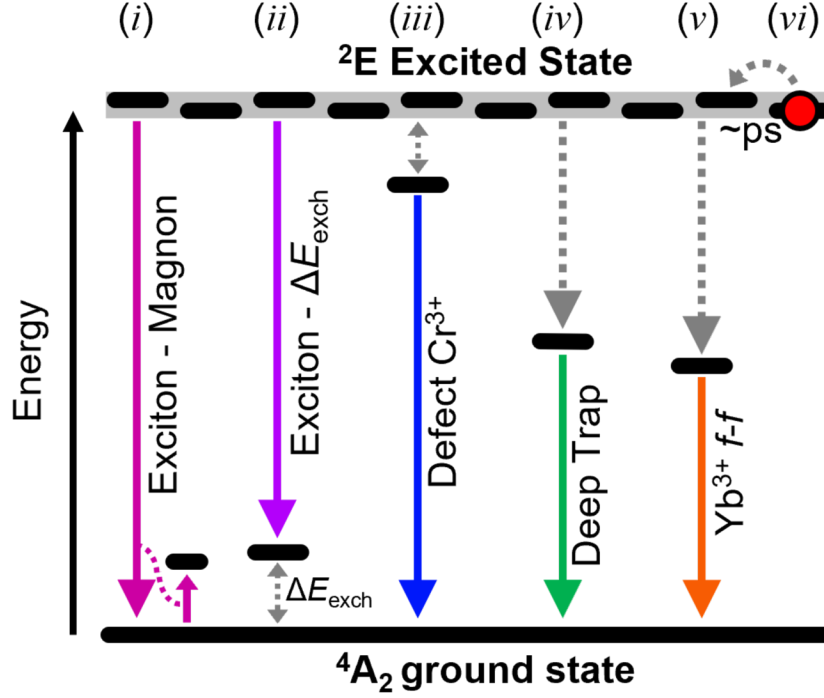
Finally, although several of the same fine-structure peaks appear in both the absorption (PLE) and PL spectra of $CrPS_4$, the PL spectrum shows an additional prominent peak at $E(^2E) - 140 \text{ cm}^{-1}$ that is absent from the PLE spectrum. This peak is also assigned as a transition that has become spin-allowed ($\Delta S = 0$) through exchange *via* the Tanabe mechanism, but in this case reflecting only short-range order. To illustrate, Figure 6d depicts the energy levels of an exchange-coupled Cr^{3+} ion relaxing from its 2E ($S = 1/2$) excited state to its 4A_2 ($S = 3/2$) ground state. Fixing all neighboring intralayer Cr^{3+} spin projections to $+3/2$ in the ordered state, ferromagnetic exchange coupling between this central ion and the surrounding Cr^{3+} ions yields the ground- and excited-state spin splittings depicted. The corresponding pair spin states (S_{pair}) involving the nearest-neighbor Cr^{3+} are also indicated. Whereas the highest-energy $^2E \rightarrow ^4A_2$ transition at low temperature (denoted $^2E(+1/2, 2) \rightarrow ^4A_2(+3/2, 3)$, with $\Delta S_{\text{pair}} = +1$) requires a spin flip and must therefore couple with other lattice spins to gain electric-dipole allowedness as described above, the next lower-energy transition ($^2E(+1/2, 2) \rightarrow ^4A_2(+1/2, 2)$, $\Delta S_{\text{pair}} = 0$) has no such restriction. The far greater intensity of this $^2E(+1/2, 2) \rightarrow ^4A_2(+1/2, 2)$ transition compared to any of the $^2E(+1/2, 2) \rightarrow ^4A_2(+3/2, 3)$ magnon sidebands demonstrates the greater efficacy of short-range order for overcoming $^2E \rightarrow ^4A_2$ spin-forbiddenness. The PL peak at $E(^2E) - 140 \text{ cm}^{-1}$ is thus assigned to transition (i) in Figure 6d, and its shift from the first electronic origin is related to the $^4A_2(+1/2, 2) - ^4A_2(+3/2, 3)$ ground-state exchange splitting. If the excited-state exchange coupling were instead antiferromagnetic, then this PL energy shift would reflect the splitting between $^4A_2(+3/2, 3)$ and $^4A_2(-1/2, 1)$ levels in Figure 6d. Notably, regardless of the sign of the excited-state exchange coupling, there is no absorption transition originating from the $^4A_2(+3/2, 3)$ low-temperature ground state that conserves spin, and hence no comparably intense magnetic sideband

in the PLE spectrum of Figure 6a. The ${}^4A_2(+1/2, 2) \rightarrow {}^2E(+1/2, 2)$ excitation should appear as a hot band, and sizeable hot-band intensity redshifted from the low-temperature origin is observed (Figure 6b), but with an energy gap of 140 cm^{-1} and T_N of only 36 K this transition would carry significant intensity only in the paramagnetic regime, where extensive broadening and other hot bands also occur. This interpretation of the $E({}^2E) - 140\text{ cm}^{-1}$ PL feature is supported by the PL temperature dependence across the magnetic ordering temperature: at T_N and above (*e.g.*, at 36 K, Figure 2), where long-range spin correlation vanishes but short-range exchange splittings remain, the magnon fine structure has broadened and disappeared whereas the ${}^2E(+1/2, 2) \rightarrow {}^4A_2(+1/2, 2)$ transition depicted in Figure 6d persists. This transition dominates the 2E PL intensity at these temperatures, serving as the magnetic "false" origin for the most prominent vibronic progression.

III. Conclusion

The low-temperature PL spectrum of the layered van der Waals magnet CrPS₄ has long been known to display extremely complex fine structure. Although to date interpreted in terms of the single-ion ligand-field model as ${}^2E \rightarrow {}^4A_2$ luminescence, the magnetic ordering of this lattice implies a role for magnetism in its PL that has not been previously accounted for. Here, we have presented PL measurements at various temperatures and in the time domain, in conjunction with absorption, PLE, and PL quantum yield measurements, that lead to several new conclusions about the optical spectroscopy and electronic structure of CrPS₄: (a) the intrinsic pure electronic transition occurs at 11069 cm^{-1} , as determined by overlap between mirror-image PL and PLE spectra at low temperature, (b) the majority of the low-energy fine structure in both PL and PLE spectra can be assigned as magnon sidebands to the formally spin-forbidden ${}^4A_2 \leftrightarrow {}^2E$ electronic transitions of lattice Cr³⁺ ions, gaining electric-dipole intensity through the Tanabe exchange mechanism, (c) the intrinsic PL intensity is dominated by a magnetic "false" origin 140 cm^{-1} below the pure electronic transition and its associated vibronic sidebands, particularly at and above T_N , whose intensity also derives from the Tanabe mechanism but involves only short-range magnetic order, (d) PL from an additional "defect" Cr³⁺ species is identified 208 cm^{-1} below the lattice Cr³⁺ PL using a combination of PLE and time-resolved PL measurements, and (e) sub-picosecond inter-site excitation hopping in CrPS₄ leads to Frenkel-type exciton formation with a small dispersion energy of $\Delta E_{\text{band}} < \sim 20\text{ cm}^{-1}$. Several of these findings are summarized in Scheme 1.

Scheme 1. Summary of the various dynamical processes occurring in CrPS₄ and Yb³⁺:CrPS₄ following photoexcitation. Straight solid arrows indicate luminescence and dashed arrows indicate nonradiative processes. The five major radiative relaxation processes are (i) ²E PL coupled to magnon excitation (magenta), (ii) ²E PL terminating in an excited spin level of the exchange-split ground state (violet), (iii) ²E PL from shallow "defect" Cr³⁺ (blue), (iv) native deep-trap PL (green), and (v) Yb³⁺ *f-f* PL in samples where Yb³⁺ has been doped into CrPS₄ (orange). (vi) shows picosecond hopping between translationally inequivalent Cr³⁺ ions.



These findings demonstrate that most of the extremely rich and unusual structure in the optical spectra of CrPS₄, as well as its *b*-axis polarization, derives directly from this lattice's magnetic structure. Whereas magnon sidebands and exchange-enhanced spin-flip transitions have been detailed previously in 3D transition-metal ionic and oxide antiferromagnets,^{58, 67, 68, 71-75, 78-80, 84} such phenomena have not been widely observed in the optical spectroscopy of van der Waals magnets. To our knowledge, the only direct observation of magnon sidebands in the optical spectrum of a 2D thiophosphate magnet comes from second-harmonic generation measurements on MnPS₃ in the region of the sharp ⁶A₁ → ⁴A₁/⁴E(G) ligand-field excitations.^{85,86} Magnon sidebands are also observed in spin-flip excitations of layered 2D metal-halide perovskites of Cr²⁺ and Mn²⁺.^{82,83,87} At the same time, magnon generation *via* optical excitation has been demonstrated in numerous related 2D materials where magnon sidebands have not been identified or assigned,

for example in the A-type antiferromagnet CrSBr.^{7,88}

As another Cr³⁺-based quasi-1D A-AFM material, CrSBr is a particularly significant comparison for this work. This material's absorption/PLE and PL have been widely described^{89,90} as involving band-to-band (single-particle) electronic transitions, but in fact the spectra are remarkably similar to those of CrPS₄. Although never described in this way before, the data and analysis presented here for CrPS₄ suggest that the emissive excited state of CrSBr could instead be a dispersive ²E ligand-field state. Three important differences between CrSBr and CrPS₄ are: (i) the stronger Cr³⁺–Cr³⁺ exchange interactions, (ii) the presence of only one Cr³⁺ lattice site, and (iii) the shorter (1- vs 3-atom) separation between 1D chains in CrSBr. If also ²E emission, these differences would cause greater ²E exciton dispersion both along and perpendicular to the primary 1D Cr³⁺ chains, and hence sizable deviation of the magnon sideband structure from the relatively unperturbed DOS energy pattern seen for CrPS₄. This comparison will be discussed further in a forthcoming report.

In conclusion, the spectroscopic results and analysis presented here shed new light on the role of magnetism in the optical transitions of CrPS₄, showing that the primary PL and absorption/PLE intensity-gaining processes all involve exchange-mediated coupling of ⁴A₂ ↔ ²E ligand-field transitions with spin-compensating changes in the ground state, involving either magnons (long-range order) or local exchange splittings (short-range order) to overcome the strict spin selection rule ($\Delta S = 0$) of the single-ion spin-flip optical transition. This study advances our understanding of the fundamental electronic structure of CrPS₄ in ways that may help inform future studies and applications of magnetic van der Waals materials as a novel class of spin-photonic materials. Furthermore, the observation of resolved magnon sidebands in the PLE spectra of CrPS₄ points to the possibility of launching magnons optically with mode selectivity, offering new avenues for optically initiated spin generation and manipulation in layered magnetic materials.

IV. Methods

Synthesis of CrPS₄ and Yb³⁺-doped CrPS₄ crystals. Crystals were grown by chemical vapor transport in a manner similar to that described previously.^{23, 40} A chromium chip (99.995%, lot MKCH4484) was purchased from Sigma Aldrich. The Cr chip was ground to a powder using a mortar and pestle. Red phosphorus powder (> 97.0%, lot MKCS0319) was purchased from Sigma Aldrich. Sulfur powder (99.98%, lot STBL3899) was purchased from Sigma Aldrich. Ytterbium metal powder 40 mesh (99.9%) was purchased from BeanTown Chemical. All chemicals were used as received without further purification. In a typical synthesis, Yb metal (x mmol), Cr metal (2.6 - x mmol), P powder (2.6 mmol in P), and S₈ powder (1.3 mmol in S) were loaded (an x :1- x :1:4 mole ratio of the elements) into a quartz tube and sealed under an evacuated atmosphere. The

quartz tubes were 10 cm long with inner and outer diameters of 14 and 16 mm, respectively. Sealed tubes were placed in an open-ended horizontal tube furnace with the starting materials in the hot zone set at 750°C and the other end at a temperature of 650°C. Samples were heated for 5 days and then allowed to cool to room temperature over a period of ca. 6 hr. Once cooled, the tubes were cracked open to yield shiny dark plate-like crystals that had formed at the cold end. Yb³⁺ doping was confirmed by inductively coupled plasma mass spectrometry (ICP-MS) using a PerkinElmer NexION 2000B. ICP-MS samples were digested in high-purity concentrated nitric acid, followed by dilution in ultrapure H₂O. Yb³⁺ doping levels (*x*) are reported as a percentage relative to the total cation content, [Yb³⁺]/([Cr³⁺]+[Yb³⁺]). Analytical Yb³⁺ concentrations were ~50 times smaller than the nominal ytterbium concentrations used in the synthesis. The measured Yb³⁺ concentrations in the flakes studied here were 0.20 ± 0.05% and 0.020 ± 0.005% with the uncertainty accounting for flake-to-flake variability. The 0.002% Yb³⁺ concentration is estimated based on the expected linear relationship between nominal concentration and analytical concentration because it was too dilute to measure. Crystal thickness was measured by mounting a flake to a glass slide using double-sided tape and imaging the edge of the flake with an optical microscope at various magnifications. The edge thickness was calculated in ImageJ2 using known pixel resolutions at several spots across the sample to obtain an average and range of thickness. CrPS₄ and 0.2% Yb³⁺:CrPS₄ microcrystal solutions were prepared by 8-hr sonication of the parent single crystals in hexane.

Magnetic measurements. Magnetic measurements were collected on an as-synthesized single crystal using a Quantum Design MPMS®3 - SQUID Magnetometer (MEM-C Shared Facilities) collecting in the vibrating sample magnetometer mode.

X-ray diffraction. As-synthesized flakes were characterized by X-ray diffraction using a Bruker D8 Discover powder diffractometer with I μ S microfocus X-ray source for Cu K α radiation (50 kV, 1 mA). Samples were placed onto crystalline silicon substrates and measured under ambient conditions.

Raman scattering. Raman measurements were performed using a Renishaw inVia Raman microscope equipped with a 1200 grooves/mm grating and a Leica DMIRBE inverted optical microscope. A 532 nm laser was used as the excitation source. The collimated monochromatic beam was focused onto the sample through a Leica objective lens. Raman-scattered light was collected by the same objective, directed into the inVia spectrometer, dispersed by the diffraction grating, and focused on a CCD camera.

Transmission electron microscopy. 8 μ L of 0.2% Yb³⁺:CrPS₄ microcrystal solution in hexane was drop-cast onto an Ultrathin Carbon Type A, 400 mesh Cu TEM grid three times, allowing the solvent to dry between drops. The grid was then dried overnight under vacuum before imaging with a Technai G2 F20 Supertwin TEM operating at 200 kV.

Photoluminescence (PL). Single crystals of the material were placed between two sapphire disks and loaded into a closed-cycle or helium immersion cryostat. Crystals were exfoliated prior to loading to ensure fresh surfaces. Measured samples were typically 100-500 μ m thick. Measurements were performed under high vacuum (10⁻⁶ Pa). Sample emission was focused into a monochromator with a spectral bandwidth of 0.05 nm (~0.5 cm⁻¹) for most measurements, and as specified in each figure. The excitation source and collection axes were both normal to the crystal face. Spectra were collected using a LN₂-cooled silicon CCD camera (measurements with < 1 nm spectral bandwidth) or a Hamamatsu InGaAs/InP NIR photomultiplier tube (measurements with \geq 1 nm spectral bandwidth). All PL spectra were corrected for instrument response. Photoexcitation was performed using either a 632.8 nm helium-neon laser, a tunable Ti:sapphire

laser, a 532 nm Nd:YAG laser, a 470 nm pulsed laser diode, a 405 nm LED, or a 375 nm pulsed laser diode as specified in the text. Where specified, polarization scrambling was achieved by passing the excitation source and sample emission through fused silica depolarizers. Unless specifically indicated otherwise, crystal orientation was not controlled relative to the excitation polarization, and the excitation source was depolarized.

Photoluminescence excitation (PLE). PLE measurements were likewise conducted in a closed-cycle helium cryostat under high vacuum. Sample emission was focused into a monochromator with a spectral bandwidth of 5 nm ($\sim 44\text{ cm}^{-1}$) for $\text{Yb}^{3+}:\text{CrPS}_4$ or 15 nm ($\sim 150\text{ cm}^{-1}$) for CrPS_4 and emission counts were monitored using a Hamamatsu InGaAs/InP NIR photomultiplier tube. Spectra were corrected for intensity of the excitation source, measured simultaneously using a calibrated Si diode. Photoexcitation was performed using either a halogen lamp coupled to a spectrometer with a 1 nm ($\sim 10\text{ cm}^{-1}$) linewidth or a tunable Ti:sapphire laser with an integration-time-limited linewidth of 0.01 nm ($\sim 0.1\text{ cm}^{-1}$). For Figures 5, S10, S11, and S28, “exfoliated 0.2% $\text{Yb}^{3+}:\text{CrPS}_4$ crystals on clear adhesive tape” were prepared by repeatedly exfoliating a 0.2% $\text{Yb}^{3+}:\text{CrPS}_4$ single crystal on the same piece of clear Scotch-brand tape until the tape was uniformly faintly orange. This piece of tape was mounted between two sapphire discs and measured as described above.

Photoluminescence quantum yield (PLQY). The PLQY was measured at room temperature for 11 different flakes, and the average was found to be $0.14 \pm 0.04\%$, accounting for flake-to-flake variation and measurement variability. Large flakes ($> 1\text{ mm}$ thick and 5 mm wide) must be used for PLQY due to the very weak luminescence, but small flakes ($< 0.5\text{ mm}$ thick and 2 mm wide) are used for low-temperature measurements to ensure effective cooling. The room-temperature PLQY is used to determine the PLQY at low temperature using the full vis-NIR spectra measured at low temperature and room temperature using a NIR PMT (Figure S13). Then, the high-resolution CCD spectra, despite missing the IR PL component, are analyzed by comparison with the low temperature PLQY in the overlapping measurement region ($\sim 9000\text{--}12000\text{ cm}^{-1}$). PLQY for just the ^2E luminescence ($\Phi_{2\text{E}}$) was determined by integrating the PL intensity from $10950\text{--}11200\text{ cm}^{-1}$ and multiplying this intensity by 8 to represent the ^2E PL (this integrated region is $\sim 7\text{--}9\times$ smaller than the entire deconvoluted ^2E PL spectrum at 1.6 and 36 K).

Spin-wave calculations. Linear spin-wave calculations were performed using SpinW.⁹¹ The crystallographic and magnetic parameters were obtained from ref 30. The Cr^{3+} spins are assigned a 9.6° off- c -axis orientation based on ref 31. The magnon density of states was generated using 56-point mesh along each axis, 800 energy bins, and a 0.1 meV (0.8 cm^{-1}) Gaussian broadening factor. All four magnetic sublattices are included.

Supplementary Materials. See Supplemental Material at [URL inserted by publisher]. 29 figures showing supplemental XRD, Raman, and magnetic susceptibility data, absorption and PL data, optical microscope and TEM images, and brief descriptions of PLQY determination and energy-hopping dynamics.

Data Availability. The original experimental data presented in this work will be made freely available at <https://doi.org/10.5281/zenodo.17643780> upon manuscript acceptance.

Acknowledgments. This research was primarily supported by the University of Washington Molecular Engineering Materials Center, a U.S. National Science Foundation Materials Research Science and Engineering Center (DMR-2308979). The work on CrPS_4 microcrystal solutions was

supported by the U.S. National Science Foundation, Division of Materials Research (solid state and materials chemistry), through award DMR-2404703. Support from an NSF Graduate Research Fellowship (1000356387) to R.T.S. is gratefully acknowledged. Part of this work was conducted at the Molecular Analysis Facility, which is supported in part by funds from the Molecular Engineering & Sciences Institute, the Clean Energy Institute, the National Science Foundation (NNCI-2025489 and NNCI-1542101). The authors thank Dr. Kimo Pressler for assistance with the optical microscope measurements, Dr. Faris Horani for Raman measurements, Thom Snoeren for ICP-MS measurements, and Nick Adams for assistance with PL measurements.

References

- (1) Wang, Q. H.; Bedoya-Pinto, A.; Blei, M.; Dismukes, A. H.; Hamo, A.; Jenkins, S.; Koperski, M.; Liu, Y.; Sun, Q.-C.; Telford, E. J.; Kim, H. H.; Augustin, M.; Vool, U.; Yin, J.-X.; Li, L. H.; Falin, A.; Dean, C. R.; Casanova, F.; Evans, R. F. L.; Chshiev, M.; *et al.* The Magnetic Genome of Two-Dimensional van der Waals Materials. *ACS Nano* **2022**, *16*, 6960–7079.
- (2) Jia, Z.; Zhao, M.; Chen, Q.; Tian, Y.; Liu, L.; Zhang, F.; Zhang, D.; Ji, Y.; Camargo, B.; Ye, K.; Sun, R.; Wang, Z.; Jiang, Y. Spintronic Devices upon 2D Magnetic Materials and Heterojunctions. *ACS Nano* **2025**, *19*, 9452–9483.
- (3) Huang, B.; Clark, G.; Navarro-Moratalla, E.; Klein, D. R.; Cheng, R.; Seyler, K. L.; Zhong, D.; Schmidgall, E.; McGuire, M. A.; Cobden, D. H.; Yao, W.; Xiao, D.; Jarillo-Herrero, P.; Xu, X. Layer-dependent ferromagnetism in a van der Waals crystal down to the monolayer limit. *Nature* **2017**, *546*, 270–273.
- (4) Son, J.; Son, S.; Park, P.; Kim, M.; Tao, Z.; Oh, J.; Lee, T.; Lee, S.; Kim, J.; Zhang, K.; Cho, K.; Kamiyama, T.; Lee, J. H.; Mak, K. F.; Shan, J.; Kim, M.; Park, J.-G.; Lee, J. Air-Stable and Layer-Dependent Ferromagnetism in Atomically Thin van der Waals CrPS₄. *ACS Nano* **2021**, *15*, 16904–16912.
- (5) Cenker, J.; Huang, B.; Suri, N.; Thijssen, P.; Miller, A.; Song, T.; Taniguchi, T.; Watanabe, K.; McGuire, M. A.; Xiao, D.; Xu, X. Direct observation of two-dimensional magnons in atomically thin CrI₃. *Nat. Phys.* **2020**, *17*, 20–25.
- (6) Chen, G.; Qi, S.; Liu, J.; Chen, D.; Wang, J.; Yan, S.; Zhang, Y.; Cao, S.; Lu, M.; Tian, S.; Chen, K.; Yu, P.; Liu, Z.; Xie, X. C.; Xiao, J.; Shindou, R.; Chen, J.-H. Electrically switchable van der Waals magnon valves. *Nat. Commun.* **2021**, *12*, 6279.
- (7) Bae, Y. J.; Wang, J.; Scheie, A.; Xu, J.; Chica, D. G.; Diederich, G. M.; Cenker, J.; Ziebel, M. E.; Bai, Y.; Ren, H.; Dean, C. R.; Delor, M.; Xu, X.; Roy, X.; Kent, A. D.; Zhu, X. Exciton-coupled coherent magnons in a 2D semiconductor. *Nature* **2022**, *609*, 282–286.
- (8) Qi, S.; Chen, D.; Chen, K.; Liu, J.; Chen, G.; Luo, B.; Cui, H.; Jia, L.; Li, J.; Huang, M.; Song, Y.; Han, S.; Tong, L.; Yu, P.; Liu, Y.; Wu, H.; Wu, S.; Xiao, J.; Shindou, R.; Xie, X. C.; *et al.* Giant electrically tunable magnon transport anisotropy in a van der Waals antiferromagnetic insulator. *Nat. Commun.* **2023**, *14*, 2526.
- (9) Tian, J.; Wang, C.; Zhou, L.; Bai, Y.; Yang, Y.; Lei, Y.; Chen, L.; Li, C.; Wang, J. Thermal magnon transport in van der Waals antiferromagnetic CrPS₄. *Appl. Phys. Lett.* **2025**, *127*, 062406.
- (10) Song, T.; Cai, X.; Tu, M. W.-Y.; Zhang, X.; Huang, B.; Wilson, N. P.; Seyler, K. L.; Zhu, L.; Taniguchi, T.; Watanabe, K.; McGuire, M. A.; Cobden, D. H.; Xiao, D.; Yao, W.; Xu, X. Giant tunneling magnetoresistance in spin-filter van der Waals heterostructures. *Science* **2018**, *360*, 1214–1218.

- (11) Fu, Z.; Huang, H.-F.; Samarawickrama, P.; Watanabe, K.; Taniguchi, T.; Wang, W.; Ackerman, J.; Zang, J.; Yu, J.-X.; Tian, J. Anomalous Tunneling Magnetoresistance Oscillation and Electrically Tunable Tunneling Anisotropic Magnetoresistance in Few-Layer CrPS₄. *Adv. Phys. Res.* **2024**, *3*, 2400052.
- (12) Yao, F.; Liao, M.; Gibertini, M.; Cheon, C.-Y.; Lin, X.; Wu, F.; Watanabe, K.; Taniguchi, T.; Gutiérrez-Lezama, I.; Morpurgo, A. F. Switching on and off the spin polarization of the conduction band in antiferromagnetic bilayer transistors. *Nat. Nanotechnol.* **2025**, *20*, 609–616.
- (13) Zhang, Z.; Shang, J.; Jiang, C.; Rasmita, A.; Gao, W.; Yu, T. Direct Photoluminescence Probing of Ferromagnetism in Monolayer Two-Dimensional CrBr₃. *Nano Lett.* **2019**, *19*, 3138–3142.
- (14) Zhang, X.-X.; Jiang, S.; Lee, J.; Lee, C.; Mak, K. F.; Shan, J. Spin Dynamics Slowdown near the Antiferromagnetic Critical Point in Atomically Thin FePS₃. *Nano Lett.* **2021**, *21*, 5045–5052.
- (15) Diederich, G. M.; Cenker, J.; Ren, Y.; Fonseca, J.; Chica, D. G.; Bae, Y. J.; Zhu, X.; Roy, X.; Cao, T.; Xiao, D.; Xu, X. Tunable interaction between excitons and hybridized magnons in a layered semiconductor. *Nat. Nanotechnol.* **2023**, *18*, 23–28.
- (16) Dirnberger, F.; Quan, J.; Bushati, R.; Diederich, G. M.; Florian, M.; Klein, J.; Mosina, K.; Sofer, Z.; Xu, X.; Kamra, A.; García-Vidal, F. J.; Alù, A.; Menon, V. M. Magneto-optics in a van der Waals magnet tuned by self-hybridized polaritons. *Nature* **2023**, *620*, 533–537.
- (17) Marques-Moros, F.; Boix-Constant, C.; Mañas-Valero, S.; Canet-Ferrer, J.; Coronado, E. Interplay between Optical Emission and Magnetism in the van der Waals Magnetic Semiconductor CrSBr in the Two-Dimensional Limit. *ACS Nano* **2023**, *17*, 13224–13231.
- (18) Matthiesen, M.; Hortensius, J. R.; Mañas-Valero, S.; Kapon, I.; Dumcenco, D.; Giannini, E.; Šiškins, M.; Ivanov, B. A.; Zant, H. S. J. v. d.; Coronado, E.; Kuzmenko, A. B.; Afanasiev, D.; Caviglia, A. D. Controlling Magnetism with Light in a Zero Orbital Angular Momentum Antiferromagnet. *Phys. Rev. Lett.* **2023**, *130*, 076702.
- (19) Khusyainov, D.; Gareev, T.; Radovskaia, V.; Sampathkumar, K.; Acharya, S.; Šiškins, M.; Mañas-Valero, S.; Ivanov, B. A.; Coronado, E.; Rasing, T.; Kimel, A. V.; Afanasiev, D. Ultrafast laser-induced spin–lattice dynamics in the van der Waals antiferromagnet CoPS₃. *APL Mater.* **2023**, *11*, 071104.
- (20) Kuntu, D. V.; Arkhipova, E. A.; Shelukhin, L. A.; Mertens, F.; Prosnikov, M. A.; Eliseyev, I. A.; Smirnov, A. N.; Davydov, V. Y.; Mañas-Valero, S.; Coronado, E.; Cinchetti, M.; Kalashnikova, A. M. Laser-induced demagnetization in van der Waals XY- and Ising-like antiferromagnets NiPS₃ and FePS₃. *Phys. Rev. Mater.* **2024**, *8*, 014408.
- (21) Zhang, P.; Chung, T.-F.; Li, Q.; Wang, S.; Wang, Q.; Huey, W. L. B.; Yang, S.; Goldberger, J. E.; Yao, J.; Zhang, X. All-optical switching of magnetization in atomically thin CrI₃. *Nat. Mater.* **2022**, *21*, 1373–1378.
- (22) Dąbrowski, M.; Guo, S.; Strungaru, M.; Keatley, P. S.; Withers, F.; Santos, E. J. G.; Hicken, R. J. All-optical control of spin in a 2D van der Waals magnet. *Nat. Commun.* **2022**, *13*, 5976.
- (23) Baillie, J. T.; Pressler, K.; Adams, N. J.; Horani, F.; Snoeren, T. J.; Beaulac, R.; Gamelin, D. R. Optical Spin Sensing and Metamagnetic Phase Control in the 2D Van der Waals Magnet Yb³⁺-Doped CrPS₄. *ACS Nano* **2025**, *19*, 34408–34417.
- (24) Bi, L.; Hu, J.; Jiang, P.; Kim, D. H.; Dionne, G. F.; Kimerling, L. C.; Ross, C. A. On-chip optical isolation in monolithically integrated non-reciprocal optical resonators. *Nat. Photon.* **2011**, *5*, 758–762.

- (25) Chen, G.; Jin, Z.; Chen, J. A review: Magneto-optical sensor based on magnetostrictive materials and magneto-optical material. *Sens. Actuator Rep.* **2023**, *5*, 100152.
- (26) Pintus, P.; Dumont, M.; Shah, V.; Murai, T.; Shoji, Y.; Huang, D.; Moody, G.; Bowers, J. E.; Youngblood, N. Integrated non-reciprocal magneto-optics with ultra-high endurance for photonic in-memory computing. *Nat. Photon.* **2024**, *19*, 54–62.
- (27) Pei, Q. L.; Luo, X.; Lin, G. T.; Song, J. Y.; Hu, L.; Zou, Y. M.; Yu, L.; Tong, W.; Song, W. H.; Lu, W. J.; Sun, Y. P. Spin dynamics, electronic, and thermal transport properties of two-dimensional CrPS₄ single crystal. *J. Appl. Phys.* **2016**, *119*, 043902.
- (28) Lee, J.; Ko, T. Y.; Kim, J. H.; Bark, H.; Kang, B.; Jung, S.-G.; Park, T.; Lee, Z.; Ryu, S.; Lee, C. Structural and Optical Properties of Single- and Few-Layer Magnetic Semiconductor CrPS₄. *ACS Nano* **2017**, *11*, 10935–10944.
- (29) Gu, P.; Tan, Q.; Wan, Y.; Li, Z.; Peng, Y.; Lai, J.; Ma, J.; Yao, X.; Yang, S.; Yuan, K.; Sun, D.; Peng, B.; Zhang, J.; Ye, Y. Photoluminescent Quantum Interference in a van der Waals Magnet Preserved by Symmetry Breaking. *ACS Nano* **2020**, *14*, 1003–1010.
- (30) Calder, S.; Haglund, A. V.; Liu, Y.; Pajeroski, D. M.; Cao, H. B.; Williams, T. J.; Garlea, V. O.; Mandrus, D. Magnetic structure and exchange interactions in the layered semiconductor CrPS₄. *Phys. Rev. B* **2020**, *102*, 024408.
- (31) Peng, Y.; Ding, S.; Cheng, M.; Hu, Q.; Yang, J.; Wang, F.; Xue, M.; Liu, Z.; Lin, Z.; Avdeev, M.; Hou, Y.; Yang, W.; Zheng, Y.; Yang, J. Magnetic Structure and Metamagnetic Transitions in the van der Waals Antiferromagnet CrPS₄. *Adv. Mater.* **2020**, *32*, 2001200.
- (32) Bud'ko, S. L.; Gati, E.; Slade, T. J.; Canfield, P. C. Magnetic order in the van der Waals antiferromagnet CrPS₄: Anisotropic *H-T* phase diagrams and effects of pressure. *Phys. Rev. B* **2021**, *103*, 224407.
- (33) Zhang, H.; Li, Y.; Hu, X.; Xu, J.; Chen, L.; Li, G.; Yin, S.; Chen, J.; Tan, C.; Kan, X.; Li, L. In-plane anisotropic 2D CrPS₄ for promising polarization-sensitive photodetection. *Appl. Phys. Lett.* **2021**, *119*, 171102.
- (34) Riesner, M.; Fainblat, R.; Budniak, A. K.; Amouyal, Y.; Lifshitz, E.; Bacher, G. Temperature dependence of Fano resonances in CrPS₄. *J. Chem. Phys.* **2022**, *156*, 054707.
- (35) Kim, S.; Yoon, S.; Ahn, H.; Jin, G.; Kim, H.; Jo, M.-H.; Lee, C.; Kim, J.; Ryu, S. Photoluminescence Path Bifurcations by Spin Flip in Two-Dimensional CrPS₄. *ACS Nano* **2022**, *16*, 16385–16393.
- (36) Hu, L.; Dong, S.; Pan, Y.; Wang, Y.; Zhai, Y.; Wang, S.; Liu, H.; Sedmidubský, D.; Sofer, Z.; Zhou, W.; Lou, W.; Chang, K.; Xiong, Q. Magnetic Order Induced Suppression of Photoluminescence in van der Waals Magnet CrPS₄. *Laser Photonics Rev.* **2025**, *19*, 2400862.
- (37) Deng, J.; Guo, J.; Hosono, H.; Ying, T.; Chen, X. Two-dimensional bipolar ferromagnetic semiconductors from layered antiferromagnets. *Phys. Rev. Mater.* **2021**, *5*, 034005.
- (38) Yan, L.; Gong, Z.; He, Q.; Shen, D.; Ge, A.; Liu, Y.; Ma, G.; Dai, Y.; Sun, L.; Zhang, S. Polarization-Dependent Nonlinear Optical Responses of CrPS₄ for Ultrafast All-Optical Switches. *Adv. Opt. Mater.* **2024**, *12*, 2401723.
- (39) Ohno, Y.; Mineo, A.; Matsubara, I. Reflection electron-energy-loss spectroscopy, x-ray-absorption spectroscopy, and x-ray photoelectron spectroscopy studies of a new type of layer compound CrPS₄. *Phys. Rev. B* **1989**, *40*, 10262–10272.
- (40) Budniak, A. K.; Killilea, N. A.; Zelewski, S. J.; Sytnyk, M.; Kauffmann, Y.; Amouyal, Y.; Kudrawiec, R.; Heiss, W.; Lifshitz, E. Exfoliated CrPS₄ with Promising Photoconductivity. *Small* **2020**, *16*, 1905924.

- (41) Susilo, R. A.; Jang, B. G.; Feng, J.; Du, Q.; Yan, Z.; Dong, H.; Yuan, M.; Petrovic, C.; Shim, J. H.; Kim, D. Y.; Chen, B. Band gap crossover and insulator–metal transition in the compressed layered CrPS₄. *npj Quantum Mater.* **2020**, *5*, 1–8.
- (42) Zhu, J.; Feng, D.; Wang, L.; Li, L.; Li, F.; Zhou, Q.; Yan, Y. Layer-dependent structural stability and electronic properties of CrPS₄ under high pressure. *Chin. Phys. B* **2025**, *34*, 066102.
- (43) Multian, V.; Wu, F.; van der Marel, D.; Ubrig, N.; Teyssier, J. Brightened Optical Transition Hinting to Strong Spin-Lattice Coupling in a Layered Antiferromagnet. *Adv. Sci.* **2025**, 2408343.
- (44) Faş, T.; Wlazło, M.; Birowska, M.; Rybak, M.; Zinkiewicz, M.; Oleschko, L.; Goryca, M.; Gondek, Ł.; Camargo, B.; Szczytko, J.; Budniak, A. K.; Amouyal, Y.; Lifshitz, E.; Suffczyński, J. Direct Optical Probing of the Magnetic Properties of the Layered Antiferromagnet CrPS₄. *Adv. Opt. Mater.* **2025**, *13*, 2402948.
- (45) Figgis, B. N.; Hitchman, M. A. *Ligand Field Theory and Its Applications*; Wiley-VCH, 1999.
- (46) Diehl, R.; Carpentier, C. D. The Crystal Structure of Chromium Thiophosphate, CrPS₄. *Acta Crystallogr. Sect. B: Struct. Crystallogr. Cryst. Chem.* **1977**, *33*, 1399–1404.
- (47) Henderson, B.; Imbusch, G. F. *Optical Spectroscopy of Inorganic Solids*; Oxford University Press, 1989.
- (48) Jara, E.; Valiente, R.; Bettinelli, M.; Rodríguez, F. Understanding the Efficiency of Mn⁴⁺ Phosphors: Study of the Spinel Mg₂Ti_{1-x}Mn_xO₄. *J. Phys. Chem. C* **2021**, *125*, 27118–27129.
- (49) Griffith, J. S. *The Theory of Transition Metal Ions*; Cambridge University Press, 1961.
- (50) Ballhausen, C. J. *Introduction to Ligand Field Theory*; McGraw-Hill, 1962.
- (51) Adachi, S. The Best Approximate Racah Parameter Ratios of $r = C/B$ for the Cr³⁺-Activated Fluoride and Oxide Phosphors. *ECS J. Solid State Sci. Technol.* **2025**, *14*, 086001.
- (52) Brik, M. G.; Camardello, S. J.; Srivastava, A. M.; Avram, N. M.; Suchocki, A. Spin-Forbidden Transitions in the Spectra of Transition Metal Ions and Nephelauxetic Effect. *ECS J. Solid State Sci. Technol.* **2016**, *5*, R3067–R3077.
- (53) Brik, M. G.; Avram, N. M.; Avram, C. N. Comparative crystal field calculations of the Cr³⁺ energy level schemes in ZnAl₂S₄ and ZnGa₂O₄. *J. Mater. Sci.: Mater. Electron.* **2007**, *20*, 30–32.
- (54) Kim, S.; Lee, J.; Lee, C.; Ryu, S. Polarized Raman Spectra and Complex Raman Tensors of Antiferromagnetic Semiconductor CrPS₄. *J. Phys. Chem. C* **2021**, *125*, 2691–2698.
- (55) Nguyen, M. H.; Son, S.; Park, G.; Na, W.; Park, J.-G.; Cheong, H. Temperature dependent Raman study of antiferromagnetic CrPS₄. *J. Mater. Chem. C* **2024**, *12*, 12468–12473.
- (56) Neal, S. N.; O’Neal, K. R.; Haglund, A. V.; Mandrus, D. G.; Bechtel, H. A.; Carr, G. L.; Haule, K.; Vanderbilt, D.; Kim, H.-S.; Musfeldt, J. L. Exploring few and single layer CrPS₄ with near-field infrared spectroscopy. *2D Mater.* **2021**, *8*, 035020.
- (57) Li, M.; Wei, X.; Xie, Q.; Chen, L.; Ma, L.; Cheng, G. Investigation on the Intrinsic Phonon Properties of CrPS₄: A Combined Raman Spectroscopy and First-Principles Calculations Study. *ACS Omega* **2025**, *10*, 31179–31186.
- (58) van der Ziel, J. P.; Van Uitert, L. G. Magnon-Assisted Chromium Emission in YCrO₃, LuCrO₃, and GdCrO₃. *J. Appl. Phys.* **1969**, *40*, 997–998.
- (59) Inokuti, M.; Hirayama, F. Influence of Energy Transfer by the Exchange Mechanism on Donor Luminescence. *J. Chem. Phys.* **1965**, *43*, 1978–1989.
- (60) Kampli, U.; Güdel, H. U. Transfer of electronic excitation energy in the antiferromagnets rubidium trichloromanganate(II), cesium trichloromanganate(II), cesium

- tribromomanganate(II), and rubidium tetrachloromanganate(II). *Inorg. Chem.* **1984**, *23*, 3479–3486.
- (61) Knochenmuss, R.; Güdel, H. U. Exciton trapping in the one-dimensional antiferromagnet $[(\text{CH}_3)_4\text{N}]\text{MnCl}_3$. *J. Chem. Phys.* **1987**, *86*, 1104–1110.
- (62) Nataf, L.; Barreda-Argüeso, J. A.; Valiente, R.; González, J.; Rodríguez, F. Effects of Cu^{2+} doping and pressure on the exchange-mediated exciton dynamics in one-dimensional $\text{N}(\text{CH}_3)_4\text{MnCl}_3$. *Phys. Rev. B* **2014**, *89*, 115120.
- (63) Pressler, K.; Gamelin, D. R. Exciton Annihilation by Lanthanide Dopants: An Atomic Probe of Sub-Diffraction Exciton Diffusion in Ferromagnetic CrI_3 . *J. Phys. Chem. C* **2025**, *129*, 11527–11537.
- (64) Stryer, L. Fluorescence Energy Transfer as a Spectroscopic Ruler. *Annu. Rev. Biochem.* **1978**, *47*, 819–846.
- (65) Lakowicz, J. R. *Principles of Fluorescence Spectroscopy*; Springer, 2006.
- (66) van der Ziel, J. P. Davydov Splitting of the ^2E Lines in Antiferromagnetic Cr_2O_3 . *Phys. Rev. Lett.* **1967**, *18*, 237.
- (67) Allen, J. W.; Macfarlane, R. M.; White, R. L. Magnetic Davydov Splittings in the Optical Absorption Spectrum of Cr_2O_3 . *Phys. Rev.* **1969**, *179*, 523.
- (68) Macfarlane, R. M.; Allen, J. W. Exciton Bands in Antiferromagnetic Cr_2O_3 . *Phys. Rev. B* **1971**, *4*, 3054.
- (69) Bohm, D. *Quantum Theory*; Dover Publications, 1951.
- (70) Förster, T. Delocalized Excitation and Excitation Transfer. 1964; pp Technical Report No. FSU–2690–2618, Florida State University, Tallahassee, Department of Chemistry.
- (71) van Gorkom, G. G. P.; Henning, J. C. M.; van Staple, R. P. Optical Spectra of Cr^{3+} Pairs in the Spinel ZnGa_2O_4 . *Phys. Rev. B* **1973**, *8*, 955.
- (72) Szymczak, H.; Wardzyński, W.; Pajczkowska, A. Optical spectrum of antiferromagnetic spinels ZnCr_2O_4 . *J. Magn. Magn. Mater.* **1980**, *15-18*, 841–842.
- (73) Miyata, A.; Ueda, H.; Ueda, Y.; Sawabe, H.; Takeyama, S. Magnetic Phases of a Highly Frustrated Magnet, ZnCr_2O_4 , up to an Ultrahigh Magnetic Field of 600 T. *Phys. Rev. Lett.* **2011**, *107*, 207203.
- (74) Schmidt, M.; Wang, Z.; Kant, C.; Mayr, F.; Toth, S.; Islam, A. T. M. N.; Lake, B.; Tsurkan, V.; Loidl, A.; Deisenhofer, J. Exciton-magnon transitions in the frustrated chromium antiferromagnets CuCrO_2 , $\alpha\text{-CaCr}_2\text{O}_4$, CdCr_2O_4 , and ZnCr_2O_4 . *Phys. Rev. B* **2013**, *87*, 224424.
- (75) Sawada, Y.; Kimura, S.; Watanabe, K.; Ueda, H. High-field optical spectroscopy of the chromium spinel CdCr_2O_4 . *J. Phys.: Conf. Ser.* **2014**, *568*, 042028.
- (76) Sugano, S.; Tanabe, Y. Optical Spectra in Magnetically Ordered Materials. In *Magnetism*, Suhl, R. a. Ed.; Vol. 1; Academic Press, 1964; pp 243–267.
- (77) Ferguson, J.; Guggenheim, H. J.; Tanabe, Y. The Effects of Exchange Interactions in the Spectra of Octahedral Manganese. II. Compounds. *J. Phys. Soc. Jpn.* **1966**, *21*, 692–704.
- (78) van der Ziel, J. P. Spectrum of Exchange Coupled Cr^{3+} Pairs in YAlO_3 . *J. Chem. Phys.* **1972**, *57*, 2442–2450.
- (79) Schenker, R.; Weihe, H.; Güdel, H. U. Exchange Interactions Derived from Electron-Transfer Processes in $[\text{Cr}_2(\text{OH})_3(\text{tmtame})_2](\text{NO}_3)_3$. *Inorg. Chem.* **1999**, *38*, 5593–5601.
- (80) Schenker, R.; Heer, S.; Güdel, H. U.; Weihe, H. Optical Dimer Excitations and Exchange Parameters in $(\text{Et}_4\text{N})_3\text{Cr}_2\text{F}_9$: First Observation of the $^4\text{A}_2 \rightarrow ^2\text{A}_1$ Transition. *Inorg. Chem.* **2001**, *40*, 1482–1488.

- (81) Robbins, D. J.; Day, P. Temperature variation of exciton-magnon absorption bands in metamagnetic transition-metal dihalides. *J. Phys. C: Solid State Phys.* **1976**, *9*, 867–882.
- (82) Day, P.; Janke, E.; Wood, T. E.; Woodward, D. Optical estimation of the zone-centre magnon gap in Rb_2CrCl_4 : a two-dimensional easy-plane ionic ferromagnet. *J. Phys. C: Solid State Phys.* **1979**, *12*.
- (83) Smith, R. T.; Walsh, K. M.; Jiang, Q.; Chu, J.-H.; Gamelin, D. R. An Air-Stable and Exfoliable Ferromagnetic Two-Dimensional Perovskite, $(\text{Phenethylammonium})_2\text{CrCl}_4$. *Chem. Mater.* **2024**, *36*, 1571–1578.
- (84) Kopteva, N. E.; Kudlacik, D.; Yakovlev, D. R.; Eremin, M. V.; Nurmukhametov, A. R.; Bayer, M.; Pisarev, R. V. Zeeman and Davydov splitting of Frenkel excitons in the antiferromagnet CuB_2O_4 . *Phys. Rev. B* **2022**, *105*, 024421.
- (85) Gnatchenko, S. L.; Kachur, I. S.; Piryatinskaya, V. G.; Vysochanskii, Y. M.; Gurzan, M. I., Exciton-magnon structure of the optical absorption spectrum of antiferromagnetic MnPS_3 . *Low Temp. Phys.* **2011**, *37*, 144–148.
- (86) Wang, Z.; Zhang, X.-X.; Shiomi, Y.; Arima, T.-h.; Nagaosa, N.; Tokura, Y.; Ogawa, N., Exciton-magnon splitting in the van der Waals antiferromagnet MnPS_3 unveiled by second-harmonic generation. *Phys. Rev. Res.* **2023**, *5*, L042032.
- (87) Kojima, N.; Ban, T.; Tsujikawa, I., Magnon Sideband of the $^4\text{T}_{2g}(^4\text{D})$ State in the Quasi Two-Dimensional Antiferromagnet $(\text{C}_2\text{H}_5\text{NH}_3)_2\text{MnCl}_4$. *J. Phys. Soc. Japan* **1978**, *44*, 923–929.
- (88) Dirnberger, F.; Terres, S.; Iakovlev, Z. A.; Mosina, K.; Sofer, Z.; Kamra, A.; Glazov, M. M.; Chernikov, A., Exciton transport driven by spin excitations in an antiferromagnet. *arXiv preprint* **2025**, arXiv:2507.07071.
- (89) Klein, J.; Pingault, B.; Florian, M.; Heißenbüttel, M.-C.; Steinhoff, A.; Song, Z.; Torres, K.; Dirnberger, F.; Curtis, J. B.; Weile, M.; Penn, A.; Deilmann, T.; Dana, R.; Bushati, R.; Quan, J.; Luxa, J.; Sofer, Z.; Alù, A.; Menon, V. M.; Wurstbauer, U.; Rohlfing, M.; Narang, P.; Lončar, M.; Ross, F. M., The Bulk van der Waals Layered Magnet CrSBr is a Quasi-1D Material. *ACS Nano* **2023**, *17*, 5316–5328.
- (90) Ziebel, M. E.; Feuer, M. L.; Cox, J.; Zhu, X.; Dean, C. R.; Roy, X., CrSBr : An Air-Stable, Two-Dimensional Magnetic Semiconductor. *Nano Lett.* **2024**, *24*, 4319–4329.
- (91) Toth, S.; Lake, B., Linear spin wave theory for single-Q incommensurate magnetic structures. *J. Phys.: Condens. Matter* **2015**, *27*, 166002.

TOC Graphic

